NASA-CR-192161

The Semi-Discrete Galerkin Finite Element Modelling of Compressible Viscous Flow Past an Airfoil

IN-02
145584
P. 80

Final Technical Report

NAG-1-1196

Principle Investigator

Andrew J. Meade, Jr.
Rice University
Department of Mechanical Engineering
and Materials Science
Houston, Texas

(NASA-CR-192161) THE SEMI-DISCRETE
GALERKIN FINITE ELEMENT MODELLING
OF COMPRESSIBLE VISCOUS FLOW PAST
AN AIRFOIL Final Technical Report,
1 Jan. - 31 Dec. 1992 (Rice Univ.)
80 p

N93-20018

Unclas

G3/02 0145584

January 1, 1992 - December 31, 1992

The Semi-Discrete Galerkin Finite Element Modelling of Compressible Viscous Flow Past an Airfoil

Final Technical Report

NAG-1-1196

Principle Investigator

Andrew J. Meade, Jr.
Rice University
Department of Mechanical Engineering
and Materials Science
Houston, Texas

January 1, 1992 - December 31, 1992

Abstract

The Semi-Discrete Galerkin Finite Element Modelling of Compressible Viscous Flow Past an Airfoil

by

Andrew J. Meade, Jr.

A method is developed to solve the two-dimensional, steady, compressible, turbulent boundary-layer equations and is coupled to an existing Euler solver for attached transonic airfoil analysis problems. The boundary-layer formulation utilizes the semi-discrete Galerkin (SDG) method to model the spatial variable normal to the surface with linear finite elements and the time-like variable with finite differences. A Dorodnitsyn transformed system of equations is used to bound the infinite spatial domain thereby permitting the use of a uniform finite element grid which provides high resolution near the wall and automatically follows boundary-layer growth. The second-order accurate Crank-Nicholson scheme is applied along with a linearization method to take advantage of the parabolic nature of the boundary-layer equations and generate a non-iterative marching routine. The SDG code can be applied to any smoothly-connected airfoil shape without modification and can be coupled to any inviscid flow solver. In this analysis, a direct viscous-inviscid interaction is accomplished between the Euler and boundary-layer codes through the application of a transpiration velocity boundary condition. Results are presented for compressible turbulent flow past NACA 0012 and RAE 2822 airfoils at various freestream Mach numbers, Reynolds numbers, and angles of attack. All results show good agreement with experiment, and the coupled code has proven to be a computationally-efficient and accurate airfoil analysis tool.

Acknowledgments

The author would like to acknowledge the work of research assistants Brad Day and Stuart Strong. Also, Dennis Allison, Richard Campbell, and Peter Hartwich of the NASA Langley Research Center are acknowledged for their guidance and assistance with the use of GAUSS2.

Table of Contents

Abstract ii
Acknowledgments iii
List of Figures vi
List of Tables viii
Nomenclature ix

1 Introduction 1

2 Finite Element Method 3
2.1 Finite Element Approximation 3
2.2 Interpolation Functions 4
2.3 Method of Weighted Residuals 6
2.3.1 Petrov-Galerkin Method 7
2.4 Semi-Discrete Galerkin Method 7
2.5 Group Finite Element Method 10

3 Boundary Layer Formulation 12
3.1 Governing Equations 12
3.2 Traditional Dorodnitsyn Formulation 14
3.3 Semi-Discrete Galerkin Formulation 18
3.4 Self-Similar Solutions 25
3.4.1 Momentum Similarity 26
3.4.2 Energy Similarity 27
3.5 Turbulence Models 27

4 Viscous-Inviscid Interaction 30
4.1 Viscous-Inviscid Coupling 30
4.1.1 Displacement Thickness 31
4.1.2 Transpiration Velocity 32

4.2 Euler Equation Solver 33
4.2.1 Viscous-Inviscid Interfaces 34

5 Numerical Results 35
5.1 Convergence Properties 35
5.2 Flat Plate 35
5.3 NACA 0012 Airfoil 37
5.3.1 NACA 0012 - Case A 38
5.3.2 NACA 0012 - Case B 40
5.3.3 Aerodynamic Characteristics 40
5.4 RAE 2822 Airfoil 44
5.4.1 RAE 2822 - Case A 46
5.4.2 RAE 2822 - Case B 49
5.4.3 RAE 2822 - Case C 51
5.5 Grid Refinement Study 51
5.6 Aerodynamic Force Coefficients 53

6 Conclusions 56

A Galerkin Integrals 57

Bibliography 61

List of Figures

2.1 Finite Element Representation of $\phi(x)$ 4

2.2 Linear Interpolation Function $N_i^{(e)}(x)$ 5

3.1 Airfoil Coordinate System 18

3.2 Computational Plane 19

4.1 Viscous-Inviscid Interaction Scheme 31

4.2 Viscous Flow Momentum Defect 32

5.1 Nondimensional Shear Stress Convergence Results for a Flat Plate at $M_\infty = 0.800$, $Re = 5000$ 36

5.2 Comparison of Computed and Exact Nondimensional Shear Stress Profiles for a Flat Plate at $x = 0.5$, $M_\infty = 0.800$, $Re = 5000$ 37

5.3 3 and 9-Node Comparison of Computed and Exact Skin Friction for a Flat Plate at $M_\infty = 0.800$, $Re = 5000$ 38

5.4 NACA 0012 C-Grid used by GAUSS2 39

5.5 Comparison of Pressure Coefficient Distribution for the NACA 0012 Airfoil at $M_\infty = 0.499$, $\alpha_{num} = -0.14$, $Re = 9.0 \times 10^6$ 41

5.6 Skin Friction Coefficient Distribution for the NACA 0012 Airfoil Upper-Surface at $M_\infty = 0.499$, $\alpha_{num} = -0.14$, $Re = 9.0 \times 10^6$ 41

5.7 Upper-Surface Displacement Thickness for the NACA 0012 Airfoil at $M_\infty = 0.499$, $\alpha_{num} = -0.14$, $Re = 9.0 \times 10^6$ 42

5.8 Comparison of Pressure Coefficient Distribution for the NACA 0012 Airfoil at $M_\infty = 0.700$, $\alpha_{num} = 1.37$, $Re = 9.0 \times 10^6$ 42

5.9 Skin Friction Coefficient Distribution for the NACA 0012 Airfoil Upper-Surface at $M_\infty = 0.700$, $\alpha_{num} = 1.37$, $Re = 9.0 \times 10^6$ 43

5.10 Upper-Surface Displacement Thickness for the NACA 0012 Airfoil at $M_\infty = 0.700$, $\alpha_{num} = 1.37$, $Re = 9.0 \times 10^6$ 43

5.11 Comparison of Lift Coefficient vs. Angle of Attack for the NACA 0012 Airfoil at $M_\infty = 0.700$, $Re = 9.0 \times 10^6$ 44

5.12 Comparison of Lift vs. Drag Polars for the NACA 0012 Airfoil at $M_\infty = 0.700$, $Re = 9.0 \times 10^6$ 45

5.13 Comparison of Computed and Measured Transonic Drag-Rise Characteristics for the NACA 0012 Airfoil at $\alpha_{num} = 0$, $Re = 9.0 \times 10^6$. 45

5.14 Comparison of Pressure Coefficient Distribution for the RAE 2822 Airfoil at $M_\infty = 0.676$, $\alpha_{num} = -2.18$, $Re = 5.7 \times 10^6$ 47

5.15 Comparison of Upper-Surface Skin Friction Coefficient for the RAE 2822 Airfoil at $M_\infty = 0.676$, $\alpha_{num} = -2.18$, $Re = 5.7 \times 10^6$ 47

5.16 Upper-Surface Displacement Thickness Comparison for the RAE 2822 Airfoil at $M_\infty = 0.676$, $\alpha_{num} = -2.18$, $Re = 5.7 \times 10^6$ 48

5.17 Comparison of Computed and Measured Velocity Profiles for the RAE 2822 Airfoil at $M_\infty = 0.676$, $\alpha_{num} = -2.18$, $Re = 5.7 \times 10^6$ 48

5.18 Comparison of Pressure Coefficient Distribution for the RAE 2822 Airfoil at $M_\infty = 0.676$, $\alpha_{num} = 1.90$, $Re = 5.7 \times 10^6$ 49

5.19 Comparison of Upper-Surface Skin Friction Coefficient for the RAE 2822 Airfoil at $M_\infty = 0.676$, $\alpha_{num} = 1.90$, $Re = 5.7 \times 10^6$ 50

5.20 Upper-Surface Displacement Thickness Comparison for the RAE 2822 Airfoil at $M_\infty = 0.676$, $\alpha_{num} = 1.90$, $Re = 5.7 \times 10^6$ 50

5.21 Comparison of Pressure Coefficient Distribution for the RAE 2822 Airfoil at $M_\infty = 0.725$, $\alpha_{num} = 2.10$, $Re = 6.5 \times 10^6$ 51

5.22 Comparison of Upper-Surface Skin Friction Coefficient for the RAE 2822 Airfoil at $M_\infty = 0.725$, $\alpha_{num} = 2.10$, $Re = 6.5 \times 10^6$ 52

5.23 Upper-Surface Displacement Thickness Comparison for the RAE 2822 Airfoil at $M_\infty = 0.725$, $\alpha_{num} = 2.10$, $Re = 6.5 \times 10^6$ 52

5.24 Comparison of Lift Coefficient vs. Boundary-Layer Space Width for the NACA 0012 Airfoil - Case A 53

5.25 Comparison of Drag Coefficient vs. Average Grid Spacing for the NACA 0012 Airfoil - Case A 54

List of Tables

4.1 Viscous-Inviscid Variable Conversion 34

5.1 NACA 0012 Test Cases 40
5.2 RAE 2822 Test Cases 46
5.3 Force Coefficient Comparison 55

Nomenclature

Symbol	Definition
a	speed of sound
$b1, ..., b6$	nodal variables defined by Eqns. 3.37-3.42
c_p	specific heat at constant pressure
c_v	specific heat at constant volume
f	weighting function
h	height
m	Falkner-Skan pressure gradient coefficient
p	pressure
s	dependent variable defined by Eqn. 3.21
u	velocity component tangential to body surface
$\hat{u}$	normalized velocity component tangential to body surface
v	velocity component normal to body surface
v_t	transpiration velocity normal to body surface
$\hat{w}$	intermediate dependent Dorodnitsyn variable
x	coordinate tangential to body surface
y	coordinate normal to body surface
C_0	Chapman-Rubesin constant
$C_1, ..., C_4$	variable coefficients defined by Eqns. 3.47-3.48, 3.57-3.58
C_f	coefficient of friction
C_L	coefficient of lift
C_{Dp}	coefficient of drag due to pressure
C_{Dv}	coefficient of drag due to friction
C_D	total coefficient of drag
C_p	coefficient of pressure
$F1, F2$	right-hand-side of Eqns. 3.61, 3.68
FT, FS	load vectors defined by Eqns. 3.66, 3.72
H	stagnation enthalpy
$K1, ..., K10$	Galerkin integrals defined by Eqns. 3.44-3.46, 3.50-3.56

KT, KS	stiffness matrices defined by Eqns. 3.65,3.71
L	characteristic body dimension
N	interpolation function
M	total number of nodes
Pr	Prandtl number
Re	Reynolds number based on length
T	temperature
α	similarity parameter, angle of attack in degrees
β	Falkner-Skan pressure-gradient parameter
δ	boundary-layer thickness
δ^*	displacement thickness
γ	ratio of specific heats
η	independent Dorodnitsyn transformation variable
θ	implicitness factor, local body angle
λ	error tolerance
μ	kinematic viscosity
μ_t	eddy viscosity
ξ	independent Dorodnitysn transformation variable
ρ	density
σ	viscosity parameter defined in Eqn. 3.19
τ	dependent variable defined by Eqn. 3.26
ω	viscous-coupling relaxation parameter
Δ	space width
Ψ	dependent momentum similarity variable
Ω	dependent energy similarity variable

Superscript	**Definition**
n	streamwise location
q	viscous-inviscid iteration location
$\bar{}$	dimensional variable
$\tilde{}$	time-averaged variable
$*$	critical condition
$'$	fluctuating variable, derivative
$+$	eddy-viscosity mixing-length parameters

Subscript	**Definition**
e	boundary-layer edge condition
$exact$	exact value
exp	experimental value
i, j, k	indices
num	numerical value
o	stagnation condition
rms	average discrete root-mean-square
w	wall condition
∞	freestream condition

Chapter 1

Introduction

The successful application of computational fluid dynamics to the design and analysis of two-dimensional airfoils in transonic flow regimes has been accomplished by a large number of researchers in the past fifteen years. Analysis of the entire flowfield around wing sections can generally be performed through the use of two main techniques. The first technique is to solve some practical form of the Navier-Stokes equations for the entire flowfield. The second technique involves the solution of the boundary-layer equations in the viscous flowfield region and either the potential or Euler equations in the inviscid flowfield region. Iteratively solving the viscous and inviscid equations while enforcing a compatibility condition then yields a solution for the entire flowfield.

The Navier-Stokes methods, while modelling most of the physical flow mechanisms and providing accurate results, require large amounts of computer time and storage. The coupled viscous-inviscid methods are generally 30-500 times faster than the Navier-Stokes methods and generate results of adequate accuracy [33]. Advances in computer hardware technology are constantly narrowing the computational advantage held by coupled methods over the Navier-Stokes methods. However, coupled methods should continue to be particularly important in an interactive airfoil design environment where near real-time flowfield analysis is desired.

The numerical solution of the classical boundary-layer equations has traditionally been accomplished through the use of finite differences [1]. The finite element method has been used only since 1972 to obtain numerical boundary-layer solutions, even though the method itself has been in existence since 1915 [11]. Traditionally, the finite element treatment of two-dimensional boundary-layer flow has involved the use of finite differences in the streamwise direction to capitalize on the parabolic nature of the boundary-layer equations. Coordinate transformations, which reduce the number of dependent variables or generate computational grids suited for finite elements, have also been used.

In 1960, A.A. Dorodnitsyn developed and applied a set of boundary-layer transformations which are well-adapted to the finite element method of solution [15]. Initially, the transformations were used along with the method of integral relations to solve various classes of supersonic boundary-layer flows [2]. Fletcher and Fleet successfully applied the finite element method to the laminar and turbulent incompressible Dorodnitsyn form of the boundary-layer equations [3], [18]. Meade and Strong have extended the method to solve laminar compressible flow about cones and airfoils, respectively [17], [4].

Prandtl proposed that the inviscid pressure distribution could be determined to a higher-order accuracy by recalculating the potential flow while accounting for the displacement thickness of the boundary layer [5]. Perhaps the most notable transonic airfoil analysis code, employing Prandtl's direct interaction procedure to couple Green's [6] lag-entrainment boundary-layer code with an inviscid full-potential code, is the viscous Garabedian and Korn program developed by Collyer and Lock [7]. Another notable example is the GRUMFOIL program developed by Melnik, Chow, Mead, and Jameson [8]. A great deal of research has been performed to develop viscous-inviscid coupling mechanisms which do not have the disadvantages associated with the direct displacement thickness approach. The transpiration velocity boundary condition, as suggested by Lighthill [24], has been used as the viscous-inviscid coupling mechanism by Van Dalsem, Steger, and Rao with success [26].

The viscous, compressible, transonic airfoil analysis method presented in this text is based on the direct viscous-inviscid interaction of finite element boundary layer and finite difference Euler codes. The present work extends the semi-discrete Galerkin (SDG) boundary-layer formulation to include turbulent flow. A direct transpiration velocity viscous-inviscid interaction approach will be used to couple the SDG method with an innovative Euler solver (GAUSS2) which employs a shock fitting technique. The coupled codes will be used to analyze flow about a NACA 0012 and RAE 2822 airfoil for attached, turbulent, compressible flow.

Chapter 2

Finite Element Method

The finite element method is a numerical analysis technique for obtaining piecewise approximate solutions to the governing equations of a wide variety of engineering problems. The principle of the finite element method is to replace a continuum, having an infinite number of unknowns, with a discretized domain of assembled elements, having a finite number of unknowns. The unknown field variable is expressed in terms of assumed approximating functions within each element. The approximating, or interpolation, functions are defined in terms of field variable values at specific points or nodes. Each element has a prescribed number of nodes which may be on the boundary, where connections to other elements are made, or in the interior of the element. Thus, the nodal values of the field variable and the interpolation functions completely define the behavior of the field variable within the elements.

The solution to any continuum problem by the finite element method is accomplished in the following steps [10]:

- Discretize the continuum
- Select interpolation functions
- Find the element properties
- Assemble the element properties to obtain the system of equations
- Solve the system equations

2.1 Finite Element Approximation

Consider $\check{\phi}(x)$ as an approximate, or trial, solution to the one-dimensional field variable $\phi(x)$, which can be written as

$$\check{\phi}(x) = \sum_{i=1}^{M} N_i(x)\phi_i, \tag{2.1}$$

where ϕ_i are the nodal unknowns, $N_i(x)$ are the interpolation functions, and M is the total number of nodes or nodal unknowns. The derivative of $\phi(x)$ is approximated in this finite element representation by

$$\frac{d\check{\phi}}{dx} = \sum_{i=1}^{M} \frac{dN_i}{dx}\phi_i. \tag{2.2}$$

Referring to Figure 2.1, it can be seen that when linear interpolation functions N_i are used, $\check{\phi}(x)$ interpolates the function $\phi(x)$ linearly over each element.

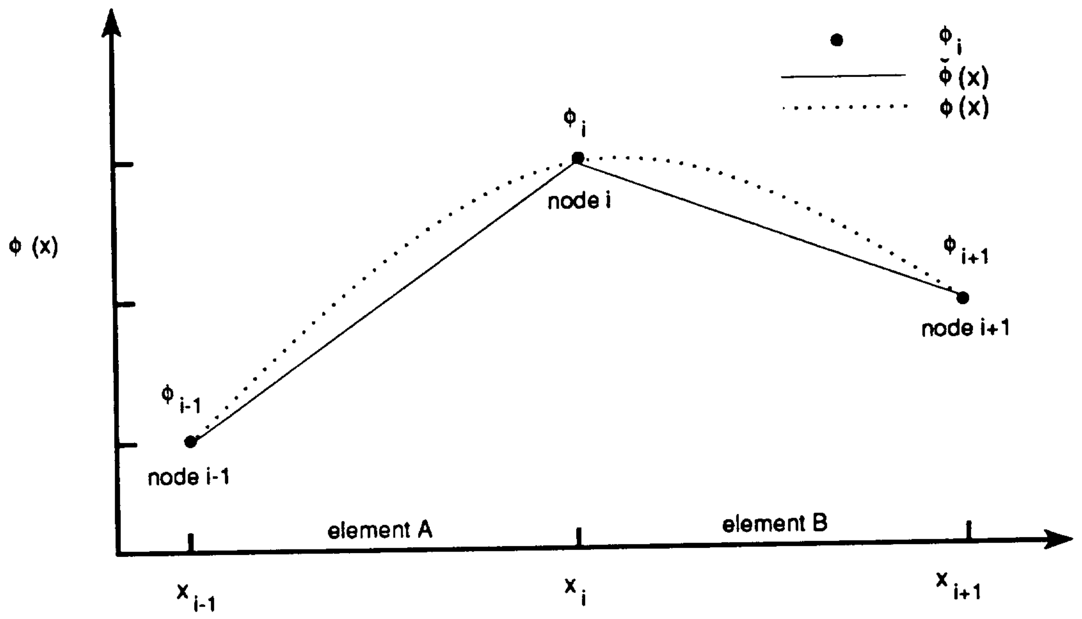

Figure 2.1 Finite Element Representation of $\phi(x)$

2.2 Interpolation Functions

Interpolation functions are normally chosen to be locally defined polynomials within each element. It can be seen from Figure 2.2 that linear interpolation functions fall from a maximum value of one at a particular node to zero at the two neighboring nodes and are zero throughout the rest of the domain. Therefore, even though Equation 2.1 is a global equation, only two nodal unknowns and two interpolation functions make a nonzero contribution in any particular element. As shown in Figure 2.2, the local shape functions satisfy the following conditions in each element (e):

$$N_i^{(e)}(x) = 0 \quad \text{if } x \text{ not in element } (e)$$
$$\sum_{i=1}^{M} N_i^{(e)}(x) = 1 \quad \text{for all } x \text{ in element } (e)$$

It is also necessary that the interpolation functions be chosen in such a way that the field variable $\phi(x)$ and any of its derivatives, up to one order less than the highest order derivative appearing in the weak form of the equation, be continuous at the element boundaries [11]. The linear interpolation functions can be determined by using Lagrange polynomials and, for elements A and B, take the form

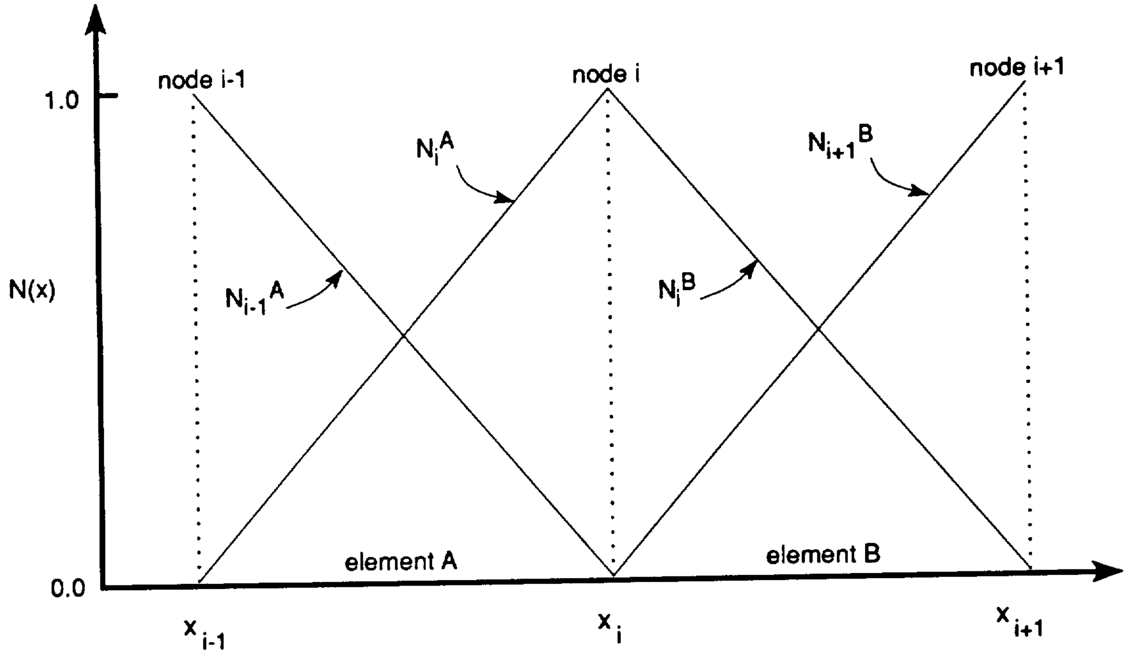

Figure 2.2 Linear Interpolation Function $N_i^{(e)}(x)$

$$N_{i-1}^A = \frac{x - x_i}{x_{i-1} - x_i} \qquad N_i^A = \frac{x - x_{i-1}}{x_i - x_{i-1}}$$
$$N_i^B = \frac{x - x_{i+1}}{x_i - x_{i+1}} \qquad N_{i+1}^B = \frac{x - x_i}{x_{i+1} - x_i}. \tag{2.3}$$

2.3 Method of Weighted Residuals

The method of weighted residuals is a technique for obtaining approximate solutions to partial differential equations. The method of weighted residuals is one of many approaches, namely the direct approach, the variational approach, or the energy-balance approach, used to determine the finite element matrix equations which express the properties of individual elements.

Applying the method of weighted residuals involves basically two steps. The first step is to assume the general functional behavior of the dependent field variable so that the given differential equation and boundary conditions are approximately satisfied. A residual, which is required to vanish over the entire solution domain, results when the approximation is substituted into the original differential equation and boundary conditions. The second step is to solve the equation(s) resulting from step one for a particular function.

Consider finding an approximate functional representation for the field variable ϕ which is governed by the differential equation

$$L(\phi) - f = 0, \tag{2.4}$$

where L represents the differential operator and f is a known function of the independent variables. The differential equation resides in the domain D bounded by the surface S, where proper boundary conditions are prescribed. The unknown exact solution for ϕ can be approximated by $\check{\phi}$ as

$$\phi \approx \check{\phi} = \sum_{i=1}^{M} N_i \phi_i, \tag{2.5}$$

where N_i are the assumed functions and ϕ_i are the unknown parameters. The M functions N_i are usually chosen to satisfy the global boundary conditions.

When $\check{\phi}$ is substituted into Equation 2.4, a residual R results from the approximation and is given by

$$R = L(\check{\phi}) - f. \tag{2.6}$$

The method of weighted residuals seeks to determine the M unknowns ϕ_i in such a way that the error R over the entire solution domain is minimized. This is accomplished by forming a weighted average of the error and specifying that this weighted average vanish over the solution domain. Therefore, choosing M linearly independent weighting functions W_j and insisting that if

$$\int_D W_j \left[L(\check{\phi}) - f\right] dD = \int_D W_j R \, dD = 0, \qquad j = 1, 2, \ldots, M \tag{2.7}$$

then $R \approx 0$. The form of error distribution principle used in Equation 2.7 is dependent on the choice of weighting function. There are a variety of weighted-residual techniques which can be employed; the most popular error distribution principle is the Galerkin Method. The Bubnov-Galerkin (classical Galerkin) method uses the interpolation functions N_j as the weighting functions W_j, while the Petrov-Galerkin method specifies W_j as some modification of N_j.

2.3.1 Petrov-Galerkin Method

The Petrov-Galerkin method is used in applications of the method of weighted residuals when specific requirements must be imposed on the finite element solution. The weighting function in this method is represented by

$$W_j = P_j, \tag{2.8}$$

where P_j is an analytic function similar to the Bubnov-Galerkin interpolation function N_j but with additional terms or factors to impose the specific solution requirements. The use of the Petrov-Galerkin method has been based in part on its ability to produce asymmetric weighting functions which force diagonal dominance of the finite element matrix equations and reduce the oscillatory solution behavior in convection-dominated fluid flows [11].

2.4 Semi-Discrete Galerkin Method

The semi-discrete Galerkin method is a hybrid finite element and finite difference numerical-analysis technique which uses a finite element representation for the spatial variables and models the time or time-like variables by finite differences. The semi-discrete Galerkin (SDG) method is best demonstrated by its application to the one-dimensional, unsteady, nondimensionalized Heat Conduction equation:

$$\frac{\partial \phi}{\partial t} - \frac{\partial^2 \phi}{\partial x^2} = 0 \tag{2.9}$$

The initial and boundary conditions for $\phi(x,t)$, over the interval $0 \leq x \leq 1$, are given by

$$\phi(x,0) = \phi_o(x), \quad \phi(0,t) = 0, \quad \phi(1,t) = 1. \tag{2.10}$$

Substituting an approximate solution for ϕ,

$$\check{\phi}(x,t) = \sum_{i=1}^{M} N_i(x)\phi_i(t), \tag{2.11}$$

into Equation 2.9 and applying the method of weighted residuals gives

$$\int_0^1 W_j \left(\frac{\partial \check{\phi}}{\partial t} - \frac{\partial^2 \check{\phi}}{\partial x^2} \right) dx = 0, \tag{2.12}$$

where $j = 1, 2, ..., M$. The classical Galerkin method can be used by taking the weighting function as the interpolation function:

$$W_j = N_j(x) \tag{2.13}$$

Therefore, Equation 2.12 becomes

$$\int_0^1 N_j \frac{\partial \check{\phi}}{\partial t} dx - \int_0^1 N_j \frac{\partial^2 \check{\phi}}{\partial x^2} dx = 0. \tag{2.14}$$

In order to satisfy the continuity requirements for linear interpolation functions, it is necessary to reduce the second partial differential by applying the Green-Gauss theorem. The Green-Gauss theorem in one-dimension is simply an integration by parts which gives

$$\int_0^1 N_j \frac{\partial \check{\phi}}{\partial t} dx = - \int_0^1 \frac{dN_j}{dx} \frac{\partial \check{\phi}}{\partial x} dx + N_j \frac{\partial \check{\phi}}{\partial x} \bigg|_0^1 . \tag{2.15}$$

The last term in Equation 2.15 represents the natural boundary conditions. If Neumann boundary conditions are present, it would be appropriate to replace the boundary term with the given condition. However, Dirichlet boundary conditions are specified so the boundary term remains incorporated in the governing equation. Substituting the approximate solutions for $\check{\phi}$ and $\frac{\partial \check{\phi}}{\partial x}$ into Equation 2.15 produces the following finite element equation:

$$\int_0^1 N_j \sum_{i=1}^{M} N_i \frac{d\phi_i}{dt} dx = - \int_0^1 \frac{dN_j}{dx} \sum_{i=1}^{M} \frac{dN_i}{dx} \phi_i dx + N_j \sum_{i=1}^{M} \frac{dN_i}{dx} \phi_i \bigg|_0^1 \tag{2.16}$$

Rewriting in a more convenient form by introducing the coefficients,

$$A1_{ji} = \int_0^1 N_j N_i dx, \qquad A2_{ji} = \int_0^1 \frac{dN_j}{dx} \frac{dN_i}{dx} dx,$$

gives

$$\sum_{i=1}^{M} A1_{ji} \frac{d\phi_i}{dt} = - \sum_{i=1}^{M} A2_{ji} \phi_i + N_j \sum_{i=1}^{M} \frac{dN_i}{dx} \phi_i \bigg|_0^1 . \tag{2.17}$$

A time-independent discretization in x (uniform) allows the solution of $A1$ and $A2$ to be obtained prior to the rest of the the solution process. The elements of matrices $A1$ and $A2$ can be solved exactly by Gaussian quadrature if lower-order polynomials are chosen as interpolation functions. Also, the matrices become tridiagonal if the interpolation functions are chosen to be linear. Modifying $A2$ to absorb the natural boundary conditions and renaming as $A3$ result in the following system of ODE's:

$$\sum_{i=1}^{M} A1_{ji}\frac{d\phi_i}{dt} = -\sum_{i=1}^{M} A3_{ji}\phi_i \tag{2.18}$$

The boundary conditions in nodal form are given by

$$\phi_1 = 0, \qquad \phi_M = 1.$$

To utilize the parabolic nature of the governing equations, a marching routine is invoked by using a finite difference discretization for $\frac{d\phi_i}{dt}$,

$$\frac{\phi_i^{n+1} - \phi_i^n}{t^{n+1} - t^n} = \frac{\Delta\phi_i^{n+1}}{\Delta t}, \tag{2.19}$$

where n denotes the time level. The resulting $\Delta\phi_i^{n+1}$ may then be solved for using the theta method:

$$\sum_{i=1}^{M} A1_{ji}\Delta\phi_i^{n+1} = -\Delta t\left[\theta\sum_{i=1}^{M} A3_{ji}\phi_i^{n+1} + (1-\theta)\sum_{i=1}^{M} A3_{ji}\phi_i^n\right] \tag{2.20}$$

The value of θ controls the degree of implicitness. A number of schemes which depend on the value of theta may be employed:

$\theta = 0.0$	fully-explicit Euler forward
$\theta = 1.0$	fully-implicit Euler backward
$\theta = 0.5$	second-order accurate Crank-Nicholson

Choosing the Crank-Nicholson technique and linearizing Equation 2.20 converts the system of ordinary differential equations into a system of linear algebraic equations given by

$$\sum_{i=1}^{M} \left(A1_{ji} + \theta\Delta t A3_{ji}\right)\Delta\phi_i^{n+1} = -\Delta t\sum_{i=1}^{M} A3_{ji}\phi_i^n. \tag{2.21}$$

A detailed discussion of the linearization is given in Section 3.3.

The right-hand side of Equation 2.21 is known for a given time increment Δt and initial condition ϕ_i^n. The left-hand side array forms a tridiagonal matrix of size $(M \times M)$ that may be efficiently solved by the Thomas Algorithm which is ideally suited for equations of this type [13]. The Thomas Algorithm requires an order of M operations $(O(M))$ which is more efficient than the $O(M^2)$ operations necessary for Gaussian elimination. After the system of equations has been solved, $\Delta\phi_i^{n+1}$ is added to the known value ϕ_i^n to give ϕ_i^{n+1}. The marching routine continues as ϕ_i^{n+1} is used in the right-hand side of the equation to solve for $\Delta\phi_i^{n+1}$ at the next time step. The time step is varied to obtain a desired accuracy, instead of performing iterations, which results in a computationally efficient algorithm.

2.5 Group Finite Element Method

Finite element treatment of the nonlinear convective terms, which are present in most flow problems, is traditionally accomplished by the introduction of a separate approximate solution for each contributing variable in the nonlinear terms. The group finite element method permits the nonlinear convective terms to be represented without introducing a separate approximate solution for each variable. Since the added connectivity of separate approximate solutions is avoided, the group finite element formulation can model nonlinear terms and avoid having products of nodal values over all connected nodes in a particular element [12].

The group finite element method consists of transforming any convective terms into a divergence form and then employing supplementary solutions for these terms. The group method is best demonstrated by its application to the one-dimensional, unsteady, nondimensionalized Burger's equation:

$$\frac{\partial\phi}{\partial t} + \phi\frac{\partial\phi}{\partial x} = \frac{1}{Re}\frac{\partial^2\phi}{\partial x^2} \tag{2.22}$$

Transforming the convective term into a divergence form,

$$\phi\frac{\partial\phi}{\partial x} = \frac{1}{2}\frac{\partial(\phi^2)}{\partial x}, \tag{2.23}$$

and substituting into Equation 2.22 gives

$$\frac{\partial\phi}{\partial t} + \frac{1}{2}\frac{\partial(\phi^2)}{\partial x} = \frac{1}{Re}\frac{\partial^2\phi}{\partial x^2}. \tag{2.24}$$

The supplemental approximate solution is then introduced for the group ϕ^2 as

$$\check{\phi}^2(x,t) = \sum_{i=1}^{M} N_i(x)\phi_i^2(t). \tag{2.25}$$

After substituting the supplemental approximate solution into Equation 2.24 and applying Galerkin's method with linear elements on a uniform grid, the following system of ODE's is produced:

$$\frac{\partial}{\partial t}\left(\frac{1}{6}\phi_{i-1}+\frac{2}{3}\phi_i+\frac{1}{6}\phi_{i+1}\right)+\frac{1}{2}\left(\phi_{i-1}+\phi_{i+1}\right)\frac{\phi_{i+1}-\phi_{i-1}}{2\Delta x} = \frac{1}{Re}\left(\frac{\phi_{i-1}-2\phi_i+\phi_{i+1}}{\Delta x^2}\right) \tag{2.26}$$

The traditional finite element formulation produced the following similar system of ODE's:

$$\frac{\partial}{\partial t}\left(\frac{1}{6}\phi_{i-1}+\frac{2}{3}\phi_i+\frac{1}{6}\phi_{i+1}\right)+\frac{1}{3}\left(\phi_{i-1}+\phi_i+\phi_{i+1}\right)\frac{\phi_{i+1}-\phi_{i-1}}{2\Delta x} = \frac{1}{Re}\left(\frac{\phi_{i-1}-2\phi_i+\phi_{i+1}}{\Delta x^2}\right) \tag{2.27}$$

As seen in the second term of Equations 2.26 and 2.27, the group method produces a computationally more economical finite element form of Burger's equation by reducing the nodal connectivity of the convective term. The group finite element method becomes progressively more economical as the order of nonlinearity or the number of dimensions increases and generally produces a more accurate finite element scheme [12].

Chapter 3

Boundary Layer Formulation

The boundary-layer approximation of the Navier-Stokes equations is valid if the viscous flow region, prior to separation from a body, is assumed to be thin. That is, the boundary-layer thickness is much smaller than the characteristic length of the body in question. Prandtl proposed that the following assumptions could be made about thin shear layer flows [14]:

- negligible body forces
- negligible normal viscous stresses
- negligible normal pressure gradient
- normal velocity ≪ tangential velocity
- tangential velocity gradients ≪ normal velocity gradients

3.1 Governing Equations

The equations of motion for steady, compressible, and turbulent boundary-layer flow are given in terms of dimensional variables:

Continuity:

$$\frac{\partial}{\partial \bar{x}}\left(\bar{\bar{\rho}}\tilde{\bar{u}}\right) + \frac{\partial}{\partial \bar{y}}\left(\widetilde{\overline{\bar{\rho}\bar{v}}}\right) = 0 \tag{3.1}$$

Momentum:

$$\bar{\bar{\rho}}\tilde{\bar{u}}\frac{\partial \tilde{\bar{u}}}{\partial \bar{x}} + \widetilde{\overline{\bar{\rho}\bar{v}}}\frac{\partial \tilde{\bar{u}}}{\partial \bar{y}} = -\frac{\partial \bar{\bar{p}}}{\partial \bar{x}} + \frac{\partial}{\partial \bar{y}}\left[\left(\bar{\mu} + \bar{\mu}_t\right)\frac{\partial \tilde{\bar{u}}}{\partial \bar{y}}\right] \tag{3.2}$$

Energy:

$$\bar{\bar{\rho}}\tilde{\bar{u}}\frac{\partial \bar{H}}{\partial \bar{x}} + \widetilde{\overline{\bar{\rho}\bar{v}}}\frac{\partial \bar{H}}{\partial \bar{y}} = \frac{1}{Pr}\frac{\partial}{\partial \bar{y}}\left[\left(\bar{\mu} + \bar{\mu}_t\right)\frac{\partial \bar{H}}{\partial \bar{y}}\right] + \left(1 - \frac{1}{Pr}\right)\frac{\partial}{\partial \bar{y}}\left[\left(\bar{\mu} + \bar{\mu}_t\right)\frac{\partial}{\partial \bar{y}}\left(\frac{\tilde{\bar{u}}^2}{2}\right)\right] \tag{3.3}$$

The Prandtl number is assumed constant, and the perfect gas assumption serves as the equation of state of the fluid. The gross effects of turbulence in the boundary layer are accounted for using the eddy-viscosity model

$$\bar{\tilde{\mu}}_t \frac{\partial \bar{\tilde{u}}}{\partial \bar{y}} = -\bar{\rho}\widetilde{\bar{u}'\bar{v}'}, \tag{3.4}$$

where the tilde denotes average values and the prime denotes fluctuating values [9]. Dropping the tilde and prime notation, the dimensional velocity components are denoted as $\bar{u}$ in the local $\bar{x}$ coordinate and $\bar{v}$ in the local $\bar{y}$ coordinate. The dimensional pressure, density, laminar viscosity, turbulent viscosity, and total enthalpy are shown as $\bar{p}$, $\bar{\rho}$, $\bar{\mu}$, $\bar{\mu}_t$, and $\bar{H}$, respectively.

The initial conditions for velocity and temperature are provided at $\bar{x} = \bar{x}_o$ and represented by

$$\bar{u}(\bar{x}_o, \bar{y}) = \bar{u}_o(\bar{y}), \qquad \bar{v}(\bar{x}_o, \bar{y}) = \bar{v}_o(\bar{y}), \qquad \text{and} \qquad \bar{T}(\bar{x}_o, \bar{y}) = \bar{T}_o(\bar{y}), \tag{3.5}$$

where $\bar{u}_o(\bar{y})$, $\bar{v}_o(\bar{y})$, and $\bar{T}_o(\bar{y})$ are known quantities.

Boundary conditions are prescribed at $\bar{y} = 0$ and $\bar{y} = \infty$. The boundary conditions for velocity are obtained by noting the no-slip condition at the surface of the body and that the tangential velocity approaches the magnitude of the inviscid velocity at the edge of the boundary layer. The velocity boundary conditions are given by

$$\bar{u}(\bar{x}, 0) = \bar{v}(\bar{x}, 0) = 0 \quad \text{and} \quad \bar{u}(\bar{x}, \infty) = \bar{u}_e(\bar{x}), \tag{3.6}$$

where $\bar{u}_e(\bar{x})$ is the velocity at the edge of the boundary layer obtained from a solution of the inviscid equations of motion. The heat-transfer boundary conditions for temperature are given by

$$\bar{T}(\bar{x}, 0) = \bar{T}_w(\bar{x}) \quad \text{and} \quad \bar{T}(\bar{x}, \infty) = \bar{T}_e(\bar{x}), \tag{3.7}$$

where w and e denote wall and boundary-layer edge conditions, respectively. If an adiabatic wall is prescribed, the following boundary conditions for temperature are required:

$$\left.\frac{\partial \bar{T}}{\partial \bar{x}}\right|_{\bar{y}=0} = 0 \quad \text{and} \quad \bar{T}(\bar{x}, \infty) = \bar{T}_e(\bar{x}) \tag{3.8}$$

The equations of motion, Equations 3.1-3.3, can be nondimensionalized by employing a characteristic length $\bar{L}$, critical speed of sound $\bar{a}^*$, and free-stream density $\bar{\rho}_\infty$. The dimensionless variables are defined as follows:

$$x = \frac{\bar{x}}{\bar{L}} \quad y = \frac{\bar{y}}{\bar{L}} \quad u = \frac{\bar{u}}{\bar{a}^*} \quad v = \frac{\bar{v}}{\bar{a}^*}$$

$$p = \frac{\bar{p}}{\bar{\rho}_\infty \bar{a}^{*2}} \quad \rho = \frac{\bar{\rho}}{\bar{\rho}_\infty} \quad \mu = \frac{\bar{\mu}}{\bar{\rho}_\infty \bar{a}^* \bar{L}} \quad H = \frac{c_p \bar{T} + \frac{1}{2}(\bar{u}^2 + \bar{v}^2)}{\bar{a}^{*2}} \tag{3.9}$$

After substitution of the nondimensionalized parameters and simplifying, the continuity equation becomes

$$\frac{\partial}{\partial x}(\rho u) + \frac{\partial}{\partial y}(\rho v) = 0. \tag{3.10}$$

Since pressure is only a function of x and is transmitted unchanged through the boundary layer,

$$\frac{\partial p}{\partial x} = \frac{dp}{dx} = \frac{dp_e}{dx},$$

where p_e is the dimensionless pressure at the edge of the boundary layer. Substituting the pressure term along with the nondimensionalized parameters into the momentum equation gives

$$\rho u \frac{\partial u}{\partial x} + \rho v \frac{\partial u}{\partial y} = -\frac{dp_e}{dx} + \frac{\partial}{\partial y}\left[(\mu + \mu_t)\frac{\partial u}{\partial y}\right]. \tag{3.11}$$

Similarly, the energy equation takes the form

$$\rho u \frac{\partial H}{\partial x} + \rho v \frac{\partial H}{\partial y} = \frac{1}{Pr}\frac{\partial}{\partial y}\left[(\mu + \mu_t)\frac{\partial H}{\partial y}\right] + \left(1 - \frac{1}{Pr}\right)\frac{\partial}{\partial y}\left[(\mu + \mu_t)\frac{\partial}{\partial y}\left(\frac{u^2}{2}\right)\right]. \tag{3.12}$$

3.2 Traditional Dorodnitsyn Formulation

A. A. Dorodnitsyn applied the method of integral relations to the compressible boundary-layer equations and transformed them into a form resembling the incompressible equations [15]. Dorodnitsyn used the following expressions to transform the body-normal x and y coordinate system to a ξ and η computational plane and smooth both velocity and density over the boundary layer:

$$\xi = \frac{1}{u_\infty p_\infty} \int_0^x u_e p_e dx \tag{3.13}$$

$$\eta = \frac{u_e}{(u_\infty \mu_\infty)^{\frac{1}{2}}} \int_0^y \rho dy \tag{3.14}$$

The Dorodnitsyn formulation utilized a normalized velocity $\hat{u}$

$$\hat{u} = \frac{u}{u_e}, \tag{3.15}$$

and an intermediate variable $\hat{w}$ given by

$$\hat{w} = \hat{u}\frac{u_\infty p_\infty}{u_e p_e}\frac{\partial \eta}{\partial x} + \left(\frac{u_\infty}{\mu_\infty}\right)^{\frac{1}{2}} \frac{v}{u_e}\frac{T_\infty}{T}. \tag{3.16}$$

Employing the Dorodnitsyn relations results in the following form of the continuity equation:

$$\frac{\partial \hat{u}}{\partial \xi} + \frac{\partial \hat{w}}{\partial \eta} = 0 \tag{3.17}$$

It is assumed that the variation of laminar viscosity across the boundary layer can be represented by the linear relation

$$\frac{\mu}{\mu_\infty} = C_0\frac{T}{T_\infty}, \tag{3.18}$$

where C_0 is the Chapman-Rubesin constant. A full explanation of the assumption is given in Reference [16]. Applying the Chapman-Rubesin relation, ideal-gas law, Dorodnitsyn relations, and a viscosity parameter σ

$$\sigma = 1 + \frac{\mu_t}{\mu}, \tag{3.19}$$

results in the following form of the momentum equation:

$$\hat{u}\frac{\partial \hat{u}}{\partial \xi} + \hat{w}\frac{\partial \hat{u}}{\partial \eta} = \frac{1}{u_e}\frac{du_e}{d\xi}\left(1 - \hat{u}^2\right) + C_0\frac{\partial}{\partial \eta}\left(\sigma\frac{\partial \hat{u}}{\partial \eta}\right) \tag{3.20}$$

Using a new variable s which relates enthalpy and the ratio of specific heats ($\gamma = c_p/c_v$)

$$s = \left[1 - 2H\frac{(\gamma-1)}{(\gamma+1)}\right]\left(\frac{1}{u_e^2}\right), \tag{3.21}$$

with the Dorodnitsyn relations results in the following form of the energy equation:

$$\hat{u}\frac{\partial s}{\partial \xi} + \hat{w}\frac{\partial s}{\partial \eta} + 2\frac{1}{u_e}\frac{du_e}{d\xi}\hat{u}s = \frac{C_0}{Pr}\frac{\partial}{\partial \eta}\left(\sigma\frac{\partial s}{\partial \eta}\right) + 2C_0\frac{(\gamma-1)}{(\gamma+1)}\left(\frac{1}{Pr} - 1\right)\frac{\partial}{\partial \eta}\left(\hat{u}\sigma\frac{\partial \hat{u}}{\partial \eta}\right) \tag{3.22}$$

The Dorodnitsyn formulation, representing the two-dimensional, compressible, boundary-layer equations in incompressible form with respect to the independent variables, ξ and η, is therefore given by Equations 3.17, 3.20, and 3.22. An integral form of these equations can be obtained by applying the method of weighted residuals.

After using a general weighting function $f(\hat{u})$ and summing the products of Equation 3.17 × f and Equation 3.20 × $\frac{df}{d\hat{u}}$, the first Dorodnitsyn equation appears as

$$\frac{\partial(\hat{u}f)}{\partial \xi} + \frac{\partial(\hat{w}f)}{\partial \eta} = \frac{1}{u_e}\frac{du_e}{d\xi}\left(1 - \hat{u}^2\right)\frac{df}{d\hat{u}} + C_0\frac{df}{d\hat{u}}\frac{\partial}{\partial \eta}\left(\sigma\frac{\partial \hat{u}}{\partial \eta}\right). \tag{3.23}$$

Integrating the above equation with respect to η and reducing gives the following:

$$\frac{d}{d\xi}\int_0^\infty \hat{u} f d\eta + \hat{w} f|_0^\infty = \frac{1}{u_e}\frac{du_e}{d\xi}\int_0^\infty \left(1-\hat{u}^2\right)\frac{df}{d\hat{u}}d\eta + C_0\int_0^\infty \frac{df}{d\hat{u}}\frac{\partial}{\partial\eta}\left(\sigma\frac{\partial\hat{u}}{\partial\eta}\right)d\eta \tag{3.24}$$

Applying the Crocco transformation to the integral equation changes the independent variable η to $\hat{u}$ [17]. The transformation makes use of the nondimensionalized shear stress and is given by

$$\hat{u} = \int_0^\eta \tau d\eta, \tag{3.25}$$

or

$$\tau = \frac{\partial\hat{u}}{\partial\eta}. \tag{3.26}$$

Substituting the Crocco transformation into Equation 3.24 and noting that the limits of integration are changed from $\eta = 0 \rightarrow \infty$ to $\hat{u} = 0 \rightarrow 1$, gives

$$\frac{d}{d\xi}\int_0^1 \hat{u} f \frac{1}{\tau} d\hat{u} + \hat{w} f|_0^1 = \frac{1}{u_e}\frac{du_e}{d\xi}\int_0^1 \left(1-\hat{u}^2\right)\frac{df}{d\hat{u}}\frac{1}{\tau}d\hat{u} + C_0\int_0^1 \frac{df}{d\hat{u}}\frac{\partial}{\partial\hat{u}}(\sigma\tau)\,d\hat{u}. \tag{3.27}$$

Assuming that there is no surface injection, v, and hence $\hat{w}$, is zero at the wall. Therefore, if $f(\hat{u})$ is chosen to vanish at the edge of the boundary layer, the traditional Dorodnitsyn formulation for the first integral equation reduces to

$$\frac{d}{d\xi}\int_0^1 \hat{u} f \frac{1}{\tau} d\hat{u} = \frac{1}{u_e}\frac{du_e}{d\xi}\int_0^1 \left(1-\hat{u}^2\right)\frac{df}{d\hat{u}}\frac{1}{\tau}d\hat{u} + C_0\int_0^1 \frac{df}{d\hat{u}}\frac{\partial}{\partial\hat{u}}(\sigma\tau)\,d\hat{u}. \tag{3.28}$$

After using a general weighting function $f(\hat{u})$ and summing the products of Equation 3.17 $\times\ s \times f$, Equation 3.20 $\times\ s \times \frac{df}{d\hat{u}}$, and Equation 3.22 $\times\ f$, the second Dorodnitsyn equation appears as

$$\begin{aligned}\frac{\partial(\hat{u}fs)}{\partial\xi} + \frac{\partial(\hat{w}fs)}{\partial\eta} &= -2\frac{1}{u_e}\frac{du_e}{d\xi}\hat{u}fs + \frac{1}{u_e}\frac{du_e}{d\xi}\left(1-\hat{u}^2\right)\frac{df}{d\hat{u}}s \\ &+ C_0\frac{df}{d\hat{u}}\frac{\partial}{\partial\eta}\left(\sigma\frac{\partial\hat{u}}{\partial\eta}\right)s + \frac{C_0}{Pr}f\frac{\partial}{\partial\eta}\left(\sigma\frac{\partial s}{\partial\eta}\right) \\ &+ 2C_0\frac{(\gamma-1)}{(\gamma+1)}\left(\frac{1}{Pr}-1\right)f\frac{\partial}{\partial\eta}\left(\hat{u}\sigma\frac{\partial\hat{u}}{\partial\eta}\right).\end{aligned} \tag{3.29}$$

Integrating the above equation with respect to η and reducing gives the following:

$$\begin{aligned}\frac{d}{d\xi}\int_0^\infty \hat{u}fs d\eta + \hat{w}fs|_0^\infty &= -2\frac{1}{u_e}\frac{du_e}{d\xi}\int_0^\infty \hat{u}fs d\eta + \frac{1}{u_e}\frac{du_e}{d\xi}\int_0^\infty \left(1-\hat{u}^2\right)\frac{df}{d\hat{u}}s d\eta \\ &+ C_0\int_0^\infty \frac{df}{d\hat{u}}\frac{\partial}{\partial\eta}\left(\sigma\frac{\partial\hat{u}}{\partial\eta}\right)s d\eta + \frac{C_0}{Pr}\int_0^\infty f\frac{\partial}{\partial\eta}\left(\sigma\frac{\partial s}{\partial\eta}\right)d\eta \\ &+ 2C_0\frac{(\gamma-1)}{(\gamma+1)}\left(\frac{1}{Pr}-1\right)\int_0^\infty f\frac{\partial}{\partial\eta}\left(\hat{u}\sigma\frac{\partial\hat{u}}{\partial\eta}\right)d\eta\end{aligned} \tag{3.30}$$

Using the Green-Gauss theorem to reduce the second-order derivative of s with respect to η, and again applying the Crocco transformation while noting the previous assumptions for $f(\hat{u})$ and $\hat{w}$, gives the modified Dorodnitsyn formulation for the second integral equation:

$$\begin{aligned}\frac{d}{d\xi}\int_0^1 \hat{u}f\frac{s}{\tau}d\hat{u} &= -2\frac{1}{u_e}\frac{du_e}{d\xi}\int_0^1 \hat{u}f\frac{s}{\tau}d\hat{u} + \frac{1}{u_e}\frac{du_e}{d\xi}\int_0^1\left(1-\hat{u}^2\right)\frac{df}{d\hat{u}}\frac{s}{\tau}d\hat{u} \\ &+ C_0\int_0^1 \frac{df}{d\hat{u}}s\frac{\partial}{\partial\hat{u}}(\sigma\tau)\,d\hat{u} + \frac{C_0}{Pr}f\sigma\tau\frac{\partial s}{\partial\hat{u}}\bigg|_0^1 - \frac{C_0}{Pr}\int_0^1\frac{df}{d\hat{u}}\sigma\tau\frac{\partial s}{\partial\hat{u}}d\hat{u} \\ &+ 2C_0\frac{(\gamma-1)}{(\gamma+1)}\left(\frac{1}{Pr}-1\right)\int_0^1 \hat{u}f\frac{\partial}{\partial\hat{u}}(\sigma\tau)\,d\hat{u} \\ &+ 2C_0\frac{(\gamma-1)}{(\gamma+1)}\left(\frac{1}{Pr}-1\right)\int_0^1 f\sigma\tau d\hat{u} \qquad (3.31)\end{aligned}$$

In order to permit a more physically-oriented solution procedure, it is desirable to use the independent variable x in place of ξ. Making use of the fact that

$$\frac{d}{d\xi} = \frac{d}{dx}\frac{dx}{d\xi}, \quad \text{where} \quad \frac{dx}{d\xi} = \frac{u_\infty p_\infty}{u_e p_e},$$

Equations 3.28 and 3.31 become

$$\frac{d}{dx}\int_0^1 \hat{u}f\frac{1}{\tau}d\hat{u} = \frac{1}{u_e}\frac{du_e}{dx}\int_0^1\left(1-\hat{u}^2\right)\frac{df}{d\hat{u}}\frac{1}{\tau}d\hat{u} + C_0\frac{u_e p_e}{u_\infty p_\infty}\int_0^1\frac{df}{d\hat{u}}\frac{\partial}{\partial\hat{u}}(\sigma\tau)\,d\hat{u}, \qquad (3.32)$$

and

$$\begin{aligned}\frac{d}{dx}\int_0^1 \hat{u}f\frac{s}{\tau}d\hat{u} &= -2\frac{1}{u_e}\frac{du_e}{dx}\int_0^1 \hat{u}f\frac{s}{\tau}d\hat{u} \\ &+ \frac{1}{u_e}\frac{du_e}{dx}\int_0^1\left(1-\hat{u}^2\right)\frac{df}{d\hat{u}}\frac{s}{\tau}d\hat{u} + C_0\frac{u_e p_e}{u_\infty p_\infty}\int_0^1\frac{df}{d\hat{u}}s\frac{\partial}{\partial\hat{u}}(\sigma\tau)\,d\hat{u} \\ &+ \frac{C_0}{Pr}\frac{u_e p_e}{u_\infty p_\infty}f\sigma\tau\frac{\partial s}{\partial\hat{u}}\bigg|_0^1 - \frac{C_0}{Pr}\frac{u_e p_e}{u_\infty p_\infty}\int_0^1\frac{df}{d\hat{u}}\sigma\tau\frac{\partial s}{\partial\hat{u}}d\hat{u} \\ &+ 2C_0\frac{(\gamma-1)}{(\gamma+1)}\left(\frac{1}{Pr}-1\right)\frac{u_e p_e}{u_\infty p_\infty}\int_0^1 \hat{u}f\frac{\partial}{\partial\hat{u}}(\sigma\tau)\,d\hat{u} \\ &+ 2C_0\frac{(\gamma-1)}{(\gamma+1)}\left(\frac{1}{Pr}-1\right)\frac{u_e p_e}{u_\infty p_\infty}\int_0^1 f\sigma\tau d\hat{u}, \qquad (3.33)\end{aligned}$$

respectively.

The boundary conditions for τ and s in terms of the Dorodnitsyn formulation are given by

$$\tau(1) = 0, \quad s(0) = s_w = \left(1-\frac{T_w}{T_o}\right)\frac{1}{u_e^2}, \quad \text{and} \quad s(1) = 0, \qquad (3.34)$$

in the case of heat transfer at the wall. For an adiabatic wall, the boundary conditions for s are specified as

$$\left.\frac{\partial s}{\partial \hat{u}}\right|_{\hat{u}=0} = 0 \quad \text{and} \quad s(1) = 0. \tag{3.35}$$

Numerical experiments have shown that the solution for τ was generally inferior when a wall boundary condition was imposed; therefore, the wall boundary condition available from Equation 3.2 is not used [18].

It has been shown that the Dorodnitsyn formulation reduces the nonlinear partial differential equations governing two-dimensional, compressible, and turbulent flow to a set of uncoupled integral equations by seeking the proper weighted combinations of variables and equations. The integral equations are explicitly independent of density and represented in the independent variables x and $\hat{u}$. The transformation from a body-normal coordinate system (x and y) to a computational plane (x and $\hat{u}$) is depicted in Figures 3.1 and 3.2. One benefit of this coordinate transformation is that the infinite domain in the y direction has been replaced by a finite domain in the $\hat{u}$ direction. A greater benefit is that the uniform grid in $\hat{u}$ automatically captures downstream boundary-layer growth and spatially provides high resolution near the wall.

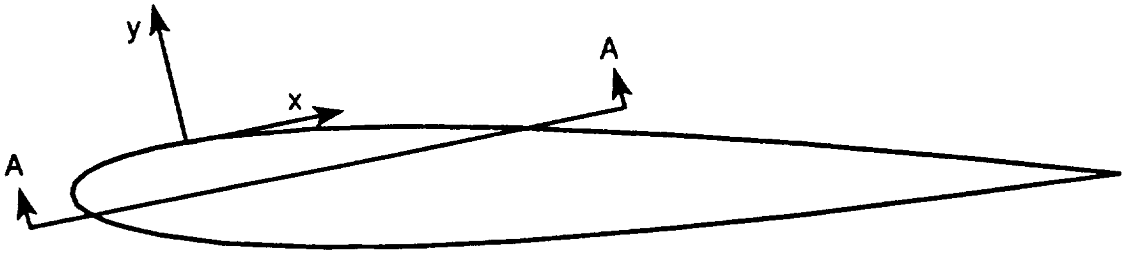

Figure 3.1 Airfoil Coordinate System

3.3 Semi-Discrete Galerkin Formulation

In order to apply the semi-discrete Galerkin method to the integral Dorodnitsyn equations developed above, the general weighting function $f(\hat{u})$ must be replaced by a set of linearly independent functions $f_j(\hat{u})$. The weighting function is introduced as

$$f_j(\hat{u}) = (1-\hat{u})N_j(\hat{u}), \qquad j = 1, 2, ..., M \tag{3.36}$$

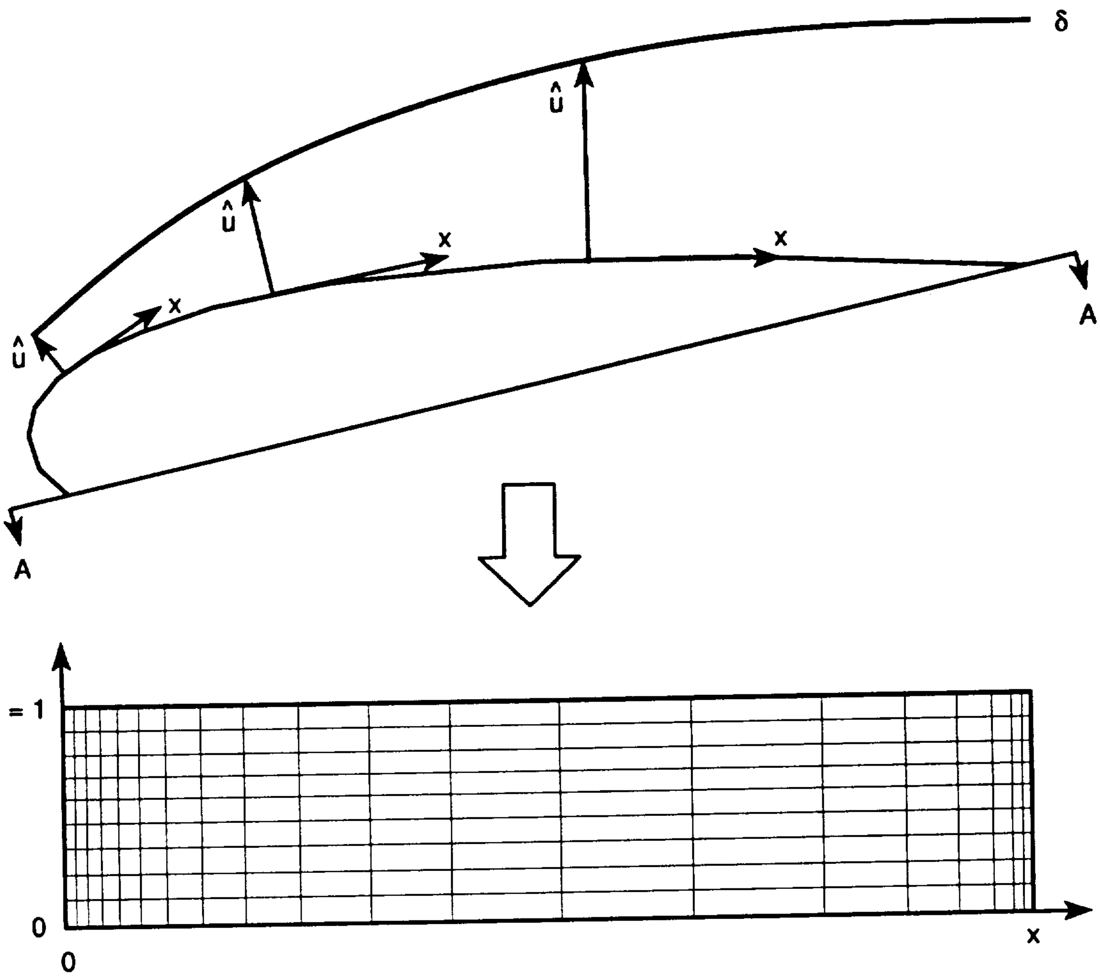

Figure 3.2 Computational Plane

where $N_j(\hat{u})$ is the linear interpolation function at a particular node j, and M is the total number of nodes. The Petrov-Galerkin finite element method is utilized by introducing the term $(1-\hat{u})$ to satisfy the requirement that $f_j(\hat{u})$ equals zero at the outer edge of the boundary layer. The trial solutions for the dependent variables $\frac{1}{\tau}$, τ, s, $\frac{s}{\tau}$, σ, and $\sigma\tau$ are introduced using the group finite element method and take the following form:

$$\frac{1}{\tau} = \frac{1}{(1-\hat{u})} \sum_{i=1}^{M} N_i(\hat{u}) b1_i(x) \tag{3.37}$$

$$\tau = (1-\hat{u}) \sum_{i=1}^{M} N_i(\hat{u}) b2_i(x) \tag{3.38}$$

$$s = (1 - \hat{u}) \sum_{i=1}^{M} N_i(\hat{u}) b3_i(x) \tag{3.39}$$

$$\frac{s}{\tau} = \sum_{i=1}^{M} N_i(\hat{u}) b4_i(x) \tag{3.40}$$

$$\sigma = \sum_{i=1}^{M} N_i(\hat{u}) b5_i(x) \tag{3.41}$$

$$\sigma\tau = (1 - \hat{u}) \sum_{i=1}^{M} N_i(\hat{u}) b6_i(x) \tag{3.42}$$

Substituting the approximate solutions and the weighting function into Equation 3.32 produces the following finite element equation:

$$\begin{aligned}
&\frac{d}{dx} \int_0^1 \hat{u} \, [(1 - \hat{u}) N_j] \left[\frac{1}{(1 - \hat{u})} \sum_{i=1}^{M} N_i b1_i \right] d\hat{u} \\
= \; & \frac{1}{u_e} \frac{du_e}{dx} \int_0^1 \left(1 - \hat{u}^2\right) \left[(1 - \hat{u}) \frac{dN_j}{d\hat{u}} - N_j \right] \left[\frac{1}{(1 - \hat{u})} \sum_{i=1}^{M} N_i b1_i \right] d\hat{u} \\
+ \; & C_0 \frac{u_e p_e}{u_\infty p_\infty} \int_0^1 \left[(1 - \hat{u}) \frac{dN_j}{d\hat{u}} - N_j \right] \left[(1 - \hat{u}) \sum_{i=1}^{M} \frac{dN_i}{d\hat{u}} b6_i - \sum_{i=1}^{M} N_i b6_i \right] d\hat{u} \quad (3.43)
\end{aligned}$$

Removing all terms that are independent of $\hat{u}$ from the integral simplifies the Equation 3.43 as follows:

First term:

$$\frac{d}{dx} \int_0^1 \hat{u} \, [(1 - \hat{u}) N_j] \left[\frac{1}{(1 - \hat{u})} \sum_{i=1}^{M} N_i b1_i \right] d\hat{u} = \sum_{i=1}^{M} \int_0^1 \hat{u} N_j N_i d\hat{u} \, \frac{db1_i}{dx}$$

Second term:

$$\begin{aligned}
&\frac{1}{u_e} \frac{du_e}{dx} \int_0^1 \left(1 - \hat{u}^2\right) \left[(1 - \hat{u}) \frac{dN_j}{d\hat{u}} - N_j \right] \left[\frac{1}{(1 - \hat{u})} \sum_{i=1}^{M} N_i b1_i \right] d\hat{u} \\
= \; & \frac{1}{u_e} \frac{du_e}{dx} \sum_{i=1}^{M} \int_0^1 (1 + \hat{u}) \left[(1 - \hat{u}) \frac{dN_j}{d\hat{u}} - N_j \right] N_i d\hat{u} \; b1_i
\end{aligned}$$

Third term:

$$\begin{aligned}
&C_0 \frac{u_e p_e}{u_\infty p_\infty} \int_0^1 \left[(1 - \hat{u}) \sum_{i=1}^{M} \frac{dN_j}{d\hat{u}} - N_j \right] \left[(1 - \hat{u}) \frac{dN_i}{d\hat{u}} b6_i - \sum_{i=1}^{M} N_i b6_i \right] d\hat{u} \\
= \; & C_0 \frac{u_e p_e}{u_\infty p_\infty} \sum_{i=1}^{M} \int_0^1 \left[(1 - \hat{u}) \frac{dN_j}{d\hat{u}} - N_j \right] \left[(1 - \hat{u}) \frac{dN_i}{d\hat{u}} - N_i \right] d\hat{u} \; b6_i
\end{aligned}$$

Therefore, after introducing

$$K1_{ji} = \int_0^1 \hat{u} N_j N_i d\hat{u}, \tag{3.44}$$

$$K2_{ji} = \int_0^1 \left[(1-\hat{u})\frac{dN_j}{d\hat{u}} - N_j\right]\left[(1-\hat{u})\frac{dN_i}{d\hat{u}} - N_i\right] d\hat{u}, \tag{3.45}$$

$$K3_{ji} = \int_0^1 (1+\hat{u})\left[(1-\hat{u})\frac{dN_j}{d\hat{u}} - N_j\right] N_i d\hat{u}, \tag{3.46}$$

$$C_1 = \frac{1}{u_e}\frac{du_e}{dx}, \tag{3.47}$$

and

$$C_2 = C_0 \frac{u_e p_e}{u_\infty p_\infty} \tag{3.48}$$

into Equation 3.43, the following system of first-order ordinary differential equations is produced:

$$\sum_{i=1}^{M} K1_{ji}\,\frac{db1_i}{dx} = C_1 \sum_{i=1}^{M} K3_{ji}\,b1_i + C_2 \sum_{i=1}^{M} K2_{ji}\,b6_i \tag{3.49}$$

After substituting the approximate solutions into Equation 3.33, removing all terms that are independent of $\hat{u}$ from the integral, and introducing

$$K4_{ji} = \int_0^1 \hat{u}(1-\hat{u}) N_j N_i d\hat{u}, \tag{3.50}$$

$$K5_{ji} = \int_0^1 (1-\hat{u}^2)\left[(1-\hat{u})\frac{dN_j}{d\hat{u}} - N_j\right] N_i d\hat{u}, \tag{3.51}$$

$$K6_{ji} = \int_0^1 (1-\hat{u})^2 N_j N_i d\hat{u}, \tag{3.52}$$

$$K7_{ji} = \int_0^1 \hat{u}(1-\hat{u}) N_j \left[(1-\hat{u})\frac{dN_i}{d\hat{u}} - N_i\right] d\hat{u}, \tag{3.53}$$

$$K8_{jik} = \int_0^1 (1-\hat{u})\left[(1-\hat{u})\frac{dN_j}{d\hat{u}} - N_j\right]\left[(1-\hat{u})\frac{dN_i}{d\hat{u}} - N_i\right] N_k d\hat{u}, \tag{3.54}$$

$$K9_{jik} = \int_0^1 (1-\hat{u})\left[(1-\hat{u})\frac{dN_j}{d\hat{u}} - N_j\right] N_i \left[(1-\hat{u})\frac{dN_k}{d\hat{u}} - N_k\right] d\hat{u}, \tag{3.55}$$

$$K10_{jik} = (1-\hat{u})^2 N_j N_i \left[(1-\hat{u})\frac{dN_k}{d\hat{u}} - N_k\right], \tag{3.56}$$

$$C_3 = C_2 \frac{1}{Pr}, \tag{3.57}$$

and

$$C_4 = 2C_2\frac{(\gamma-1)}{(\gamma+1)}\left(\frac{1}{Pr}-1\right), \tag{3.58}$$

the following system of first-order ordinary differential equations is produced:

$$\begin{aligned}\sum_{i=1}^{M} K4_{ji}\,\frac{db4_i}{dx} &= -2C_1\sum_{i=1}^{M} K4_{ji}\,b4_i + C_1\sum_{i=1}^{M} K5_{ji}\,b4_i \\ &+ C_2\sum_{i=1}^{M}\sum_{k=1}^{M} K8_{jik}\,b6_i b3_k + C_3\sum_{i=1}^{M}\sum_{k=1}^{M} K10_{jik}\,b6_i b3_k\Big|_0^1 \\ &- C_3\sum_{i=1}^{M}\sum_{k=1}^{M} K9_{jik}\,b6_i b3_k + C_4\sum_{i=1}^{M} K6_{ji}\,b6_i \\ &+ C_4\sum_{i=1}^{M} K7_{ji}\,b6_i \end{aligned} \tag{3.59}$$

The Galerkin integrals ($K1, ..., K10$) are further defined in Appendix A.

The second-order Crank-Nicholson scheme, obtained by using $\theta = 0.5$, produces an efficient implicit algorithm for marching the solution in the x direction. Equation 3.49 is approximated by

$$\sum_{i=1}^{M} K1_{ji}\,\Delta b1_i^{n+1} = \Delta x\left[\theta F1_j^{n+1} + (1-\theta)F1_j^n\right], \tag{3.60}$$

where

$$F1_j = C_1\sum_{i=1}^{M} K3_{ji}\,b1_i + C_2\sum_{i=1}^{M} K2_{ji}\,b2_i, \tag{3.61}$$

and

$$\Delta b1_i^{n+1} = b1_i^{n+1} - b1_i^n. \tag{3.62}$$

The superscript n denotes a particular streamwise, or x, position.

In order to develop a non-iterative marching routine, it is necessary to linearize $F1_j^{n+1}$ by an expansion about the nth level following the approach of Briley and MacDonald [19]:

$$\begin{aligned} F1_j^{n+1} &= F1_j^n + \Delta x\left(\frac{\partial F1_j}{\partial b1_i}\right)^n \frac{\partial b1_i}{\partial x} + \dots \\ &\approx F1_j^n + \left(\frac{\partial F1_j}{\partial b1_i}\right)^n \Delta b1_i^{n+1} \end{aligned} \tag{3.63}$$

Substitution of the linearization into Equation 3.60 produces the following system of equations in $b1$:

$$\sum_{i=1}^{M} KT_{ji}\Delta b1_i^{n+1} = FT_j \tag{3.64}$$

The variables KT and FT are defined as

$$\begin{aligned} \sum_{i=1}^{M} KT_{ji} &= \sum_{i=1}^{M} K1_{ji} - \theta\Delta x \left[C_1^{n+1} \sum_{i=1}^{M} K3_{ji} \right. \\ &- \left. C_2^{n+1} \sum_{i=1}^{M} K2_{ji} \left(\frac{b5_i^n}{b1_i^2} - \frac{1}{b1_i^n} \frac{\partial b5_i^n}{\partial b1_i^n} \right) \right], \end{aligned} \tag{3.65}$$

and

$$\begin{aligned} FT_j &= \Delta x \left\{ \left[\theta C_1^{n+1} + (1-\theta) C_1^n \right] \sum_{i=1}^{M} K3_{ji}\, b1_i^n \right. \\ &+ \left. \left[\theta C_2^{n+1} + (1-\theta) C_2^n \right] \sum_{i=1}^{M} K2_{ji}\, b6_i^n \right\}. \end{aligned} \tag{3.66}$$

Similarly, applying the Crank-Nicholson scheme to Equation 3.59 gives

$$\sum_{i=1}^{M} K4_{ji}\, \Delta b4_i^{n+1} = \Delta x \left[\theta F2_j^{n+1} + (1-\theta) F2_j^n \right], \tag{3.67}$$

where

$$\begin{aligned} F2_j &= -2C_1 \sum_{i=1}^{M} K4_{ji}\, b4_i + C_1 \sum_{i=1}^{M} K5_{ji}\, b4_i \\ &+ C_2 \sum_{i=1}^{M} \sum_{k=1}^{M} K8_{jik}\, b6_i b3_k + C_3 \sum_{i=1}^{M} \sum_{k=1}^{M} K10_{jik}\, b6_i b3_k \Big|_0^1 \\ &- C_3 \sum_{i=1}^{M} \sum_{k=1}^{M} K9_{jik}\, b6_i b3_k + C_4 \sum_{i=1}^{M} K6_{ji}\, b6_i \\ &+ C_4 \sum_{i=1}^{M} K7_{ji}\, b6_i, \end{aligned} \tag{3.68}$$

and

$$\Delta b4_i^{n+1} = b4_i^{n+1} - b4_i^n. \tag{3.69}$$

Performing the same linearization technique for $F2_j^{n+1}$ as was done for $F1_j^{n+1}$ produces the following system of equations in $b4$:

$$\sum_{i=1}^{M} KS_{ji} \Delta b4_i^{n+1} = FS_j \tag{3.70}$$

The variables KS and FS are defined as

$$\sum_{i=1}^{M} KS_{ji} = \sum_{i=1}^{M} K4_{ji} - \theta\Delta x \left[-2C_1^{n+1} \sum_{i=1}^{M} K4_{ji} + C_1^{n+1} \sum_{i=1}^{M} K5_{ji} \right.$$

$$
\begin{aligned}
&+ \quad C_2^{n+1} \sum_{i=1}^{M} \sum_{k=1}^{M} K8_{jik}\, b6_i^n b2_k^n + C_3^{n+1} \sum_{i=1}^{M} \sum_{k=1}^{M} K10_{jik}\, b6_i^n b2_k^n \Big|_0^1 \\
&- \quad C_3^{n+1} \sum_{i=1}^{M} \sum_{k=1}^{M} K9_{jik}\, b6_i^n b2_k^n \Big], \qquad (3.71)
\end{aligned}
$$

and

$$
\begin{aligned}
FS_j \;=\; & \Delta x \Big\{ -2 \left[\theta C_1^{n+1} + (1-\theta) C_1^n\right] \sum_{i=1}^{M} K4_{ji}\, b4_i \\
&+ \quad \left[\theta C_1^{n+1} + (1-\theta) C_1^n\right] \sum_{i=1}^{M} K5_{ji}\, b4_i \\
&+ \quad \left[\theta C_2^{n+1} + (1-\theta) C2^n\right] \sum_{i=1}^{M} \sum_{k=1}^{M} K8_{jik}\, b6_i b3_k \\
&+ \quad \left[\theta C_3^{n+1} + (1-\theta) C_3^n\right] \sum_{i=1}^{M} \sum_{k=1}^{M} K10_{jik}\, b6_i b3_k \Big|_0^1 \\
&- \quad \left[\theta C_3^{n+1} + (1-\theta) C_3^n\right] \sum_{i=1}^{M} \sum_{k=1}^{M} K9_{jik}\, b6_i b3_k \\
&+ \quad \left[\theta C_4^{n+1} + (1-\theta) C_4^n\right] \sum_{i=1}^{M} K6_{ji}\, b6_i \\
&+ \quad \left[C_4^{n+1} + (1-\theta) C_4^n\right] \sum_{i=1}^{M} K7_{ji}\, b6_i \Big\}. \qquad (3.72)
\end{aligned}
$$

Boundary conditions for τ and s at the boundary-layer edge are automatically imposed through the use of the $(1 - \hat{u})$ term in the trial solutions. As note previously, no wall boundary condition for τ, and hence $\Delta b1_j^{n+1}$, is imposed. The boundary condition at the wall for s, and hence $\Delta b4_j^{n+1}$, is given by

$$
\Delta b4_1^{n+1} = \Delta b1_1^{n+1} s_w. \qquad (3.73)
$$

The system of equations given by Equations 3.64 and 3.70 can be solved without iteration by the Thomas algorithm at each streamwise location using a variable step size. The variable step size is based on a comparison of the linearized and nonlinearized values of $F1_j^{n+1}$ and $F2_j^{n+1}$. The maximum relative error expression is given by

$$
\begin{aligned}
\lambda = \max \Bigg| & \frac{F1_j^{n+1}(\text{linearized}) - F1_j^{n+1}(\text{nonlinearized})}{F1_j^{n+1}(\text{nonlinearized})}, \\
& \frac{F2_j^{n+1}(\text{linearized}) - F2_j^{n+1}(\text{nonlinearized})}{F2_j^{n+1}(\text{nonlinearized})} \Bigg|. \qquad (3.74)
\end{aligned}
$$

Alternately, the linearization error can be efficiently controlled by enforcing a maximum allowable ratio of $\frac{\Delta b1_i^{n+1}}{b1_i^n}$ and $\frac{\Delta b4_i^{n+1}}{b4_i^n}$. The maximum ratio expression is given by

$$\lambda = \max \left| \frac{\Delta b1_i^{n+1}}{b1_i^n}, \frac{\Delta b4_i^{n+1}}{b4_i^n} \right| . \tag{3.75}$$

Given a maximum and minimum tolerance λ_{min} and λ_{max}, respectively, the step size is modified according to the following procedure:

$\lambda_{min} \leq \lambda \leq \lambda_{max}$	step size is unchanged
$\lambda > \lambda_{max}$	step size is halved
$\lambda < \lambda_{min}$	step size is doubled

3.4 Self-Similar Solutions

The self-similar solution may be used near the leading edge to obtain the needed initial conditions. In order to solve Equation 3.64 for the shear stress at the $(n+1)^{\text{th}}$ streamwise location, it is necessary to know the shear stress at the n^{th} streamwise location. A number of techniques have been used to obtain self-similar solutions for specific geometries within certain regions. The classic Falkner-Skan and Illingworth-Stewartson series can produce self-similar solutions for stagnation point and wedge flows with heat transfer [20], [21]. This same method may be applied to the traditional Dorodnitsyn equations of motion (laminar form of Equations 3.17, 3.20, and 3.22) to provide the initial τ and s values. Even though the governing equations of interest are turbulent, the laminar self-similar solutions are valid in the region near the stagnation point where transition to turbulence has not yet occurred.

At a small distance from the stagnation point, the velocity u_e can be approximated by

$$u_e = u_\infty \xi^m, \tag{3.76}$$

where m is related to the pressure gradient coefficient β as follows:

$$\beta = \frac{2m}{m+1} \tag{3.77}$$

Also, near the stagnation point $\Delta\xi = \xi - 0$ and $\Delta x = x - 0$ such that Equation 3.13 can be written as

$$\xi = \frac{u_e p_e}{u_\infty p_\infty} x. \tag{3.78}$$

The similarity parameter α, used to reduce the number of independent variables, is given by

$$\alpha = \eta \left(\frac{m+1}{2C_0\xi} \right)^{\frac{1}{2}} . \tag{3.79}$$

3.4.1 Momentum Similarity

The development of the momentum similarity equation takes the same form as the classical development. Using the no-slip boundary condition and integrating with respect to η, the continuity equation becomes

$$\hat{w} = -\frac{\partial}{\partial \xi} \int_0^\eta \hat{u} d\eta. \tag{3.80}$$

Representing the nondimensional velocity $\hat{u}$ as

$$\hat{u} = \frac{d\Psi}{d\alpha} = \Psi', \tag{3.81}$$

and substituting into Equation 3.80 gives

$$\hat{w} = \frac{\frac{\partial^2 \alpha}{\partial \xi \partial \eta}}{\left(\frac{\partial \alpha}{\partial \eta}\right)^2} \Psi - \frac{\frac{\partial \alpha}{\partial \xi}}{\frac{\partial \alpha}{\partial \eta}} \Psi'. \tag{3.82}$$

Substituting Equations 3.81 and 3.82 into the laminar form of Equation 3.20 generates a momentum similarity equation of the following form:

$$\Psi''' + \frac{\frac{1}{u_e}\frac{du_e}{d\xi}}{C_0 \left(\frac{\partial \alpha}{\partial \eta}\right)^2} \left(1 - \Psi'^2\right) - \frac{\frac{\partial^2 \alpha}{\partial \xi \partial \eta}}{C_0 \left(\frac{\partial \alpha}{\partial \eta}\right)^3} \Psi \Psi'' = 0 \tag{3.83}$$

The coefficients are evaluated by obtaining the same form of similarity equation as White [20], which requires

$$\beta = \frac{\frac{1}{u_e}\frac{du_e}{d\xi}}{C_0 \left(\frac{\partial \alpha}{\partial \eta}\right)^2}, \tag{3.84}$$

and

$$m = \frac{C_0 \left(\frac{\partial \alpha}{\partial \eta}\right)^3}{\frac{\partial^2 \alpha}{\partial \xi \partial \eta}} - 1. \tag{3.85}$$

Therefore, the final momentum similarity equation can be written as

$$\Psi''' + \beta \left(1 - \Psi'^2\right) + \left(\frac{1}{m+1}\right) \Psi \Psi'' = 0, \tag{3.86}$$

with the following boundary conditions:

$$\Psi(0) = \Psi'(0) = 0 \quad \text{and} \quad \Psi'(\infty) = 1 \tag{3.87}$$

3.4.2 Energy Similarity

Representing the nondimensional enthalpy parameter s as

$$s = \Omega(\alpha), \tag{3.88}$$

and substituting into the laminar form of Equation 3.22 along with Equations 3.81 and 3.82 generates an energy similarity equation of the following form:

$$\Omega'' + \frac{Pr}{m+1}\Psi\Omega' - 2Pr\beta\Psi'\Omega + 2\frac{(\gamma-1)}{(\gamma+1)}(1-Pr)\left[\Psi''^2 + \Psi'\Psi'''\right] = 0 \tag{3.89}$$

The energy similarity coefficients are evaluated according to the previous definitions for β and m. Heat-transfer boundary conditions are given by

$$\Omega(0) = s_w = \left(1 - \frac{T_w}{T_o}\right)\frac{1}{u_e^2} \quad \text{and} \quad \Omega(\infty) = 0, \tag{3.90}$$

where T_w and T_o denote wall and stagnation temperatures, respectively. If an adiabatic wall condition is prescribed, the boundary conditions are given as

$$\Omega'(0) = 0 \quad \text{and} \quad \Omega(\infty) = 0. \tag{3.91}$$

Equations 3.86 and 3.89 define a two-point boundary-value problem (BVP). Using bisection for the shooting method along with a 4th-order Runge-Kutta scheme, the BVP can be solved to produce an initial set of τ and s values that can be used to begin the marching routine. The value of τ is proportional to Ψ'' and is calculated by the following equation:

$$\tau = \frac{\partial\hat{u}}{\partial\eta} = \frac{\partial\alpha}{\partial\eta}\frac{\partial\hat{u}}{\partial\alpha} = \left(\frac{(m+1)}{2C_0}\frac{u_\infty p_\infty}{u_e p_e x}\right)^{\frac{1}{2}}\Psi'' \tag{3.92}$$

3.5 Turbulence Models

A turbulent boundary layer can be regarded approximately as a composite layer made up of inner and outer regions which arise due to the different response of the fluid to shear and pressure gradients near the wall [9]. In order to determine the eddy-viscosity μ_t in the inner and outer regions, two models based on the mixing-length concept are used in the SDG formulation.

Prandtl proposed that each turbulent fluctuation could be related to a length scale and velocity gradient:

$$\bar{\mu}_t \approx \bar{\rho}\bar{l}^2\left|\frac{\partial\bar{\bar{u}}}{\partial\bar{y}}\right| \tag{3.93}$$

The mixing length $\bar{l}$ is related to the flow conditions and takes on different values in the inner and outer turbulent flow regions.

A single inner region eddy-viscosity model, which follows the form used by Cebeci-Smith, was considered in this analysis [9]. The van Driest modified mixing-length formula in terms of the Dorodnitsyn transformation is given by

$$\frac{\mu_t}{\mu} = \frac{Re^{3/2}}{C_0}\frac{p_\infty}{p_e}\frac{u_e^2}{u_\infty^2}\rho^3 l^2 \tau, \tag{3.94}$$

where l is the mixing length ($\kappa = 0.41$)

$$l = \kappa y\left(1 - e^{y^+/A^+}\right). \tag{3.95}$$

The parameter A^+ is dependent on the pressure gradient according to

$$A^+ = \frac{A_o}{(1 + 10p^+)^{\frac{1}{2}}}, \tag{3.96}$$

where $A_o = 26$,

$$p^+ = \frac{C_0}{\sqrt{Re}}\frac{p_e}{p_\infty}\frac{u_\infty}{\rho_w^2 u_\tau^3}\frac{dp_e}{dx}, \quad \text{and} \quad u_\tau = u_e\left(\frac{C_0}{\sqrt{Re}}\frac{p_e}{p_\infty}\frac{\tau_w}{\rho_w}\right)^{\frac{1}{2}}. \tag{3.97}$$

The mixing length parameter l is related to the coordinates y^+ and y which are obtained from the solution by

$$y^+ = \frac{Re}{C_0}\frac{p_\infty}{p_e}\frac{\rho_w^2 u_\tau}{u_\infty}y, \quad \text{where} \quad y = \frac{1}{\sqrt{Re}}\frac{u_\infty}{u_e}\int_0^{\hat{u}}\frac{1}{\rho\tau}d\hat{u}. \tag{3.98}$$

Two outer region eddy-viscosity formulations were considered in this analysis. The first outer region eddy-viscosity model considered is based on the form used by Cebeci and Smith [9]. The outer model is modified to account for intermittency near the edge of the boundary layer δ:

$$\frac{\mu_t}{\mu} = \frac{0.0168}{[1 + 5.5(y/\delta)^6]}\frac{Re}{C_0}\frac{p_\infty}{p_e}\frac{u_e}{u_\infty}\rho^2\delta^* \tag{3.99}$$

The second outer region eddy-viscosity model considered is based on the form developed by Baldwin and Lomax [22]. Instead of using the boundary layer and displacement thickness as parameters in the outer formulation, the Baldwin-Lomax model uses certain maximum functions occurring in the boundary layer. The eddy-viscosity relation is given by

$$\frac{\mu_t}{\mu} = \frac{0.0168\, C_{cp}}{[1 + 5.5(C_{kleb}y/y_{max})^6]}\frac{Re}{C_0}\frac{p_\infty}{p_e}\frac{F_{max}}{u_\infty}\rho^2 y_{max}, \tag{3.100}$$

where $y_{\max}$ is the value of y corresponding to $F_{\max}$. The parameters C_{cp} and C_{kleb} are calculated by the following expressions in order to fit the known properties of Coles' wake law and equilibrium pressure gradients [23]:

$$C_{\mathrm{cp}} = \frac{3 - 4C_{\mathrm{kleb}}}{2C_{\mathrm{kleb}}\left(2 - 3C_{\mathrm{kleb}} + C_{\mathrm{kleb}}^{3}\right)} \tag{3.101}$$

$$C_{\mathrm{kleb}} = \frac{2}{3} - \frac{0.01312}{0.1724 + \beta_{\tau}} \qquad \beta_{\tau} = \frac{y_{\max}}{u_{\tau}}\frac{du_{e}}{dx} \tag{3.102}$$

The choice between the inner and outer eddy-viscosity formula is made by taking the smaller value; the changeover typically occurs at $\hat{u} \approx 0.7$.

Chapter 4

Viscous-Inviscid Interaction

In many flows of practical aerodynamic interest, the effects of viscosity and turbulence are confined to a relatively thin shear layer near the airfoil surface and wake. The flow over an airfoil can therefore be divided into two regions: an inner region, where viscous effects are important, and an outer inviscid region. Modelling the viscous and inviscid flow regions separately while providing a mechanism by which each solution influences the other is called Viscous-Inviscid Interaction (VII). A VII method organizes the viscous and inviscid parts of the overall solution to interact in an iterative way so that convergence of the final solution is achieved as economically and accurately as possible. The principle interaction between the regions arises from the displacement effect of the shear layers which leads to a thickening of the equivalent body with a corresponding change in the surface pressure [24]. The resulting interaction is labeled as either weak or strong, depending on the change in pressure and the extent to which higher-order viscous effects influence the overall solution. VII, based on a direct relationship between the viscous and inviscid regions of flow, is applicable as long as the disturbances to the inviscid flow due to the viscous displacement effect are small [25].

4.1 Viscous-Inviscid Coupling

The classical interaction approach is to obtain an approximation to the inviscid flow, extract velocity and pressure from the inviscid solution, use the external conditions to obtain an approximation to the viscous flow, extract displacement thickness from the viscous solution, and use the viscous parameters to modify the original body geometry and obtain another estimate of the inviscid flow. An alternative to adding the displacement thickness distribution to the original body thickness is to impose a transpiration velocity boundary condition at the body surface. These iterative cycles, depicted in Figure 4.1, continue until the inviscid and viscous solutions are converged and compatible.

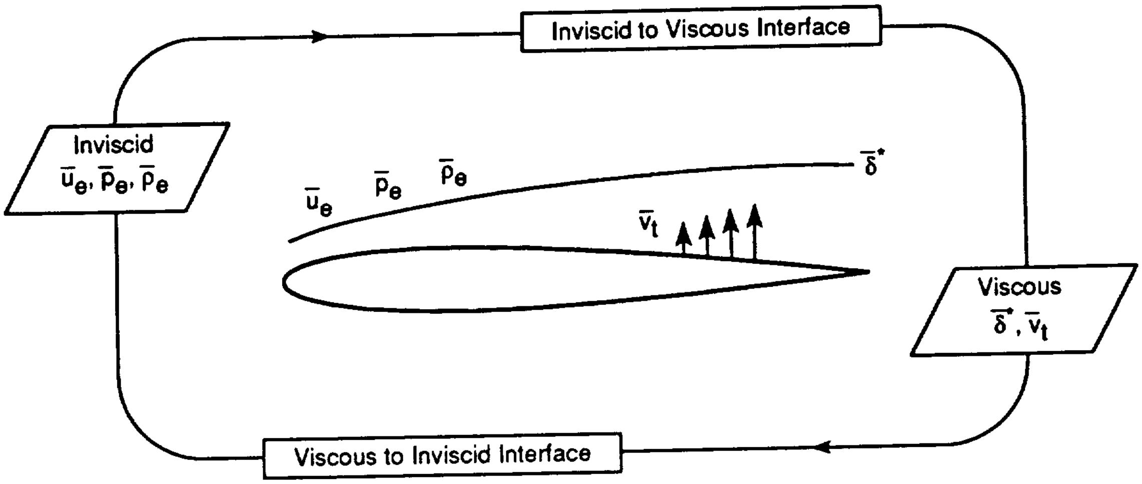

Figure 4.1 Viscous-Inviscid Interaction Scheme

4.1.1 Displacement Thickness

The displacement thickness is the height by which a streamline is displaced upward by the presence of the boundary layer. Considering the flow over a flat surface as depicted in Figure 4.2, the no-slip condition at the wall causes a partial obstruction of the freestream flow. This results in an upward deflection of the streamline passing through point $\bar{h}$ at station 1 by a distance $\bar{\delta}^*$ at station 2. Because the flat surface and the streamline form the boundaries of a streamtube, the mass flow across stations 1 and 2 must be equal and is expressed by

$$\int_0^{\bar{h}} \bar{\rho}_e \bar{u}_e d\bar{y} = \int_0^{\bar{h}} \bar{\rho}\bar{u} d\bar{y} + \bar{\rho}_e \bar{u}_e \bar{\delta}^*. \tag{4.1}$$

Rearranging gives a familiar form of the compressible displacement thickness,

$$\bar{\delta}^* = \int_0^{\bar{h}} \left(1 - \frac{\bar{\rho}\bar{u}}{\bar{\rho}_e \bar{u}_e}\right) d\bar{y}. \tag{4.2}$$

The nondimensionalized compressible displacement thickness in terms of the Dorodnitsyn formulation is given by

$$\begin{aligned} \delta^* &= \frac{(\gamma+1)}{2\gamma}\frac{1}{u_e p_e}\frac{u_\infty}{\sqrt{Re}}\int_0^1 (1-\hat{u})\frac{1}{\tau}d\hat{u} + \frac{(\gamma-1)}{2\gamma}\frac{u_e}{p_e}\frac{u_\infty}{\sqrt{Re}}\int_0^1 \hat{u}(1-\hat{u})\frac{1}{\tau}d\hat{u} \\ &- \frac{(\gamma+1)}{2\gamma}\frac{u_e}{p_e}\frac{u_\infty}{\sqrt{Re}}\int_0^1 \frac{s}{\tau}d\hat{u}. \end{aligned} \tag{4.3}$$

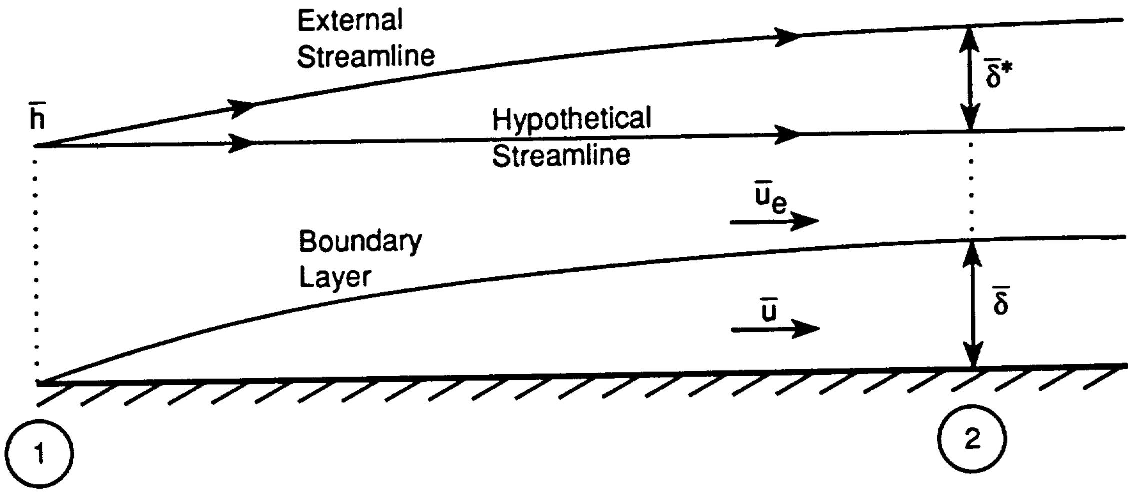

Figure 4.2 Viscous Flow Momentum Defect

The advantage of using the displacement thickness as the coupling mechanism between the viscous and inviscid solutions is its simplicity. The disadvantage of the displacement thickness approach is that the inviscid grid must be generated after each viscous iteration because the body about which the inviscid flow is computed changes when the displacement thickness alters the effective body. An additional disadvantage of the displacement thickness approach is the possibility of supercritical VII which does not allow smooth transition to separation [26]. It has been shown that the classical displacement thickness interaction becomes supercritical when $M_\infty \approx 1.5 \rightarrow 2.0$, depending on the history of the turbulent boundary layer [27].

4.1.2 Transpiration Velocity

The transpiration velocity is an inviscid normal-velocity boundary condition which is imposed at the body surface to simulate the displacement of the inviscid flow by the viscous flow momentum defect [24]. An expression for the transpiration velocity can be obtained by integrating the difference between the inviscid and viscous continuity equations across the boundary layer while applying the Prandtl boundary-layer and uniform inviscid-flow assumptions [26]. The transpiration velocity expression is given by

$$\bar{v}_t = \frac{1}{\bar{\rho}_e} \frac{\partial}{\partial \bar{x}} \left(\bar{\rho}_e \bar{u}_e \bar{\delta}^* \right) . \tag{4.4}$$

The nondimensionalized compressible transpiration velocity in terms of the Dorodnitsyn formulation is given by

$$v_t = u_e \frac{d\delta^*}{dx} + \left(\frac{du_e}{dx} + \frac{u_e}{\rho_e} \frac{d\rho_e}{dx} \right) \delta^* . \tag{4.5}$$

The transpiration velocity distribution should result in a inviscid streamline coincident with the effective body obtained with the displacement thickness approach. The advantages of the transpiration velocity approach are that the inviscid grid need not be regenerated after each viscous iteration and that the interaction always allows smooth transition to separation [27].

4.2 Euler Equation Solver

A fast and robust two-dimensional Euler code (GAUSS2), developed by Dr. Peter M. Hartwich of Vigyan Inc., is used as the inviscid flow solver in the VII scheme [28], [29]. The method uses a floating shock-fitting technique that has been combined with a second-order accurate upwind scheme based on the split-coefficient-matrix (SCM) method and with a time-implicit, diagonalized approximate-factorization (AF) algorithm. The result is a fast and robust two-dimensional Euler code that produces accurate solutions for shocked flows on crude meshes which are not adapted to the shock fronts.

The equations for two-dimensional, compressible, and nonconservative Euler equations for a polytropic gas at constant γ are given in general coordinates as

$$\mathbf{Q}_{t'} + \mathbf{A}\mathbf{Q}_{\xi'} + \mathbf{B}\mathbf{Q}_{\eta'} = \mathbf{0}, \tag{4.6}$$

where

$$\mathbf{Q} = (a', u', v', s')^T, \tag{4.7}$$

and the vectors $\mathbf{A}$ and $\mathbf{B}$ are defined by a coefficient matrix C [28]. The primes denote inviscid dependent variables where a', u', v', and s' are speed of sound, cartesian velocities, and entropy, respectively. The dependent variables have been nondimensionalized as follows:

$$x' = \frac{\bar{x}'}{\bar{L}} \quad y' = \frac{\bar{y}'}{\bar{L}} \quad u' = \frac{\bar{u}}{\sqrt{\bar{p}_\infty/\bar{\rho}_\infty}} \quad v' = \frac{\bar{v}}{\sqrt{\bar{p}_\infty/\bar{\rho}_\infty}}$$

$$a' = \frac{\bar{a}}{\sqrt{\bar{p}_\infty/\bar{\rho}_\infty}} \quad p' = \frac{\bar{p}}{\bar{p}_\infty} \quad \rho' = \frac{\bar{\rho}}{\bar{\rho}_\infty} \tag{4.8}$$

4.2.1 Viscous-Inviscid Interfaces

In order to allow the boundary-layer and Euler methods to work together in an VII scheme, it is necessary to develop a set of expressions which convert the variables from one type of nondimensionalization to another. The boundary-layer method employs a body-normal coordinate system while the Euler method employs a cartesian coordinate system, so a coordinate system conversion must be performed. Also, the methods use different reference values to nondimensionalize velocity and pressure, so a dependent variable conversion must be performed. The variable conversions which account for both the coordinate system and nondimensionalization differences are summarized in Table 4.1, where θ is the local body angle.

Table 4.1 Viscous-Inviscid Variable Conversion

Variable	Euler → Boundary Layer
Length	$x = \sqrt{x'^2 + y'^2}$
Velocity	$u = (u'\cos\theta + v'\sin\theta)\sqrt{p_\infty}$
Pressure	$p = p'p_\infty$

Chapter 5

Numerical Results

5.1 Convergence Properties

The convergence properties of the Dorodnitsyn finite element approximation of τ are plotted in Figure 5.1. The average discrete root-mean-square of the relative error is calculated by the following equation:

$$\tau_{rms} = \left[\sum_{i=1}^{M-1} \left(\frac{\tau_i}{\tau_{i,exact}} - 1 \right)^2 \right]^{\frac{1}{2}} \Big/ (M-1) \tag{5.1}$$

The exact value of τ is obtained from a solution of the similarity equations developed in Section 3.4.1 for flow over a flat plate with zero pressure gradient ($\beta = 0$). The 4th-order Runge-Kutta step size was set to $\Delta\alpha = 0.01$. The results presented in Figure 5.1 are for 8 values of $\Delta\hat{u}$ corresponding to a discretization of 3, 4, 5, 7, 9, 11, 15, and 19 nodes at $x = 0.5$ along the plate. In order to evaluate the convergence properties of the spatial discretization across the boundary layer, the step size was held at a small constant value to minimize the influence of the marching routine. Examination of the figure indicates that the use of linear elements achieves the theoretically expected second-order convergence. It can be seen that the convergence rate of the scheme decreases slightly as the number of nodes increases. The decreasing convergence rate can be attributed to the decrease in accuracy of the linearized marching scheme with increasing number of nodes. An extensive analysis of convergence properties for favorable and adverse pressure-gradient cases as well as quadratic elements may be found in Reference [18]. Fletcher and Fleet showed that the accuracy of linear elements on coarse grids are comparable to quadratic elements, and the convergence properties for the adverse and favorable pressure-gradient cases are comparable to the zero-gradient case.

5.2 Flat Plate

An assessment of the accuracy of the semi-discrete Galerkin (SDG) method may be performed by examining the ability of the method to reproduce the well-known compressible

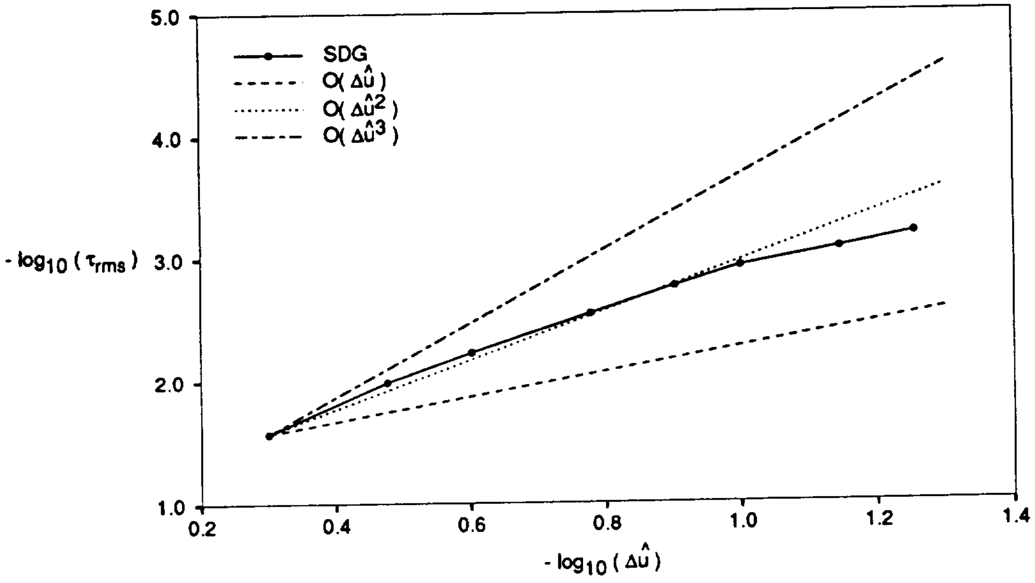

Figure 5.1 Nondimensional Shear Stress Convergence Results for a Flat Plate at $M_\infty = 0.800$, $Re = 5000$

laminar boundary-layer solution over a thermally-insulated flat plate with zero pressure gradient. The computations were performed at a Mach number of 0.8 and a Reynolds number based on plate length of 5000. A discretization of 9 nodes was used across the boundary layer. The marching routine step size was efficiently controlled by setting $\lambda_{min} = 1.0 \times 10^{-4} = 0.1\lambda_{max}$ to maintain the ratio of $\frac{\Delta b1_i^{n+1}}{b1_i^n}$ and $\frac{\Delta b4_i^{n+1}}{b4_i^n}$. Again, an exact analytical solution for this flow may be obtained by solution of the Falkner-Skan similarity equation [20]. Figure 5.2 shows excellent agreement between the exact and computed nondimensional shear-stress values at $x = 0.5$. The similarity property of the solution was also verified by examining the profiles at different stations along the length of the plate. Excellent agreement was observed except for stations close to the leading edge where effects of the stagnation-point flow are present. The skin friction along the plate was calculated using the relation

$$C_f = \frac{2C_0}{\sqrt{Re}} \frac{u_e^2}{u_\infty^2} \frac{p_e}{p_\infty} \tau_w. \tag{5.2}$$

To illustrate the high accuracy of the Dorodnitsyn formulation on extremely rough grids, both 3 and 9-node coefficient of friction solutions are plotted along with the exact solution

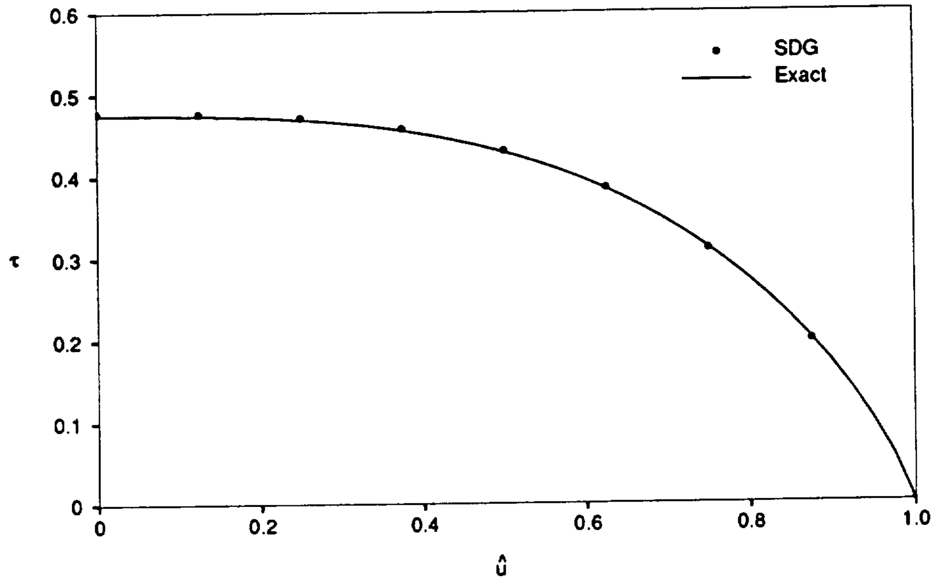

Figure 5.2 Comparison of Computed and Exact Nondimensional Shear Stress Profiles for a Flat Plate at $x = 0.5$, $M_\infty = 0.800$, $Re = 5000$

in Figure 5.3. There is excellent agreement between the 9-node and exact solutions. The 3-node solution produced good results except in the region very close to the leading edge.

5.3 NACA 0012 Airfoil

The NACA 0012 was chosen as the primary test airfoil for the compressible turbulent VII validation. The NACA 0012 is a symmetric airfoil which has been tested both computationally and experimentally by a great number of researchers. Of particular importance to the VII scheme is that the experimental data at zero angle of attack is not affected by wall interference due to lift. The airfoil is tested for attached turbulent flow at high Reynolds numbers and transonic speeds as shown in Table 5.1. In order to minimize the influence of wind tunnel wall-interference effects in the comparison of experimental and computed results, the numerical angle of attack was varied in each case to match the computed lift and the experimental normal force coefficients. In each of the NACA 0012 cases, the 161x31 C-grid shown in Figure 5.4 was used by GAUSS2 to solve the inviscid equations of motion. The outer boundary of the C-grid is located 5 to 6 chord lengths from the airfoil in

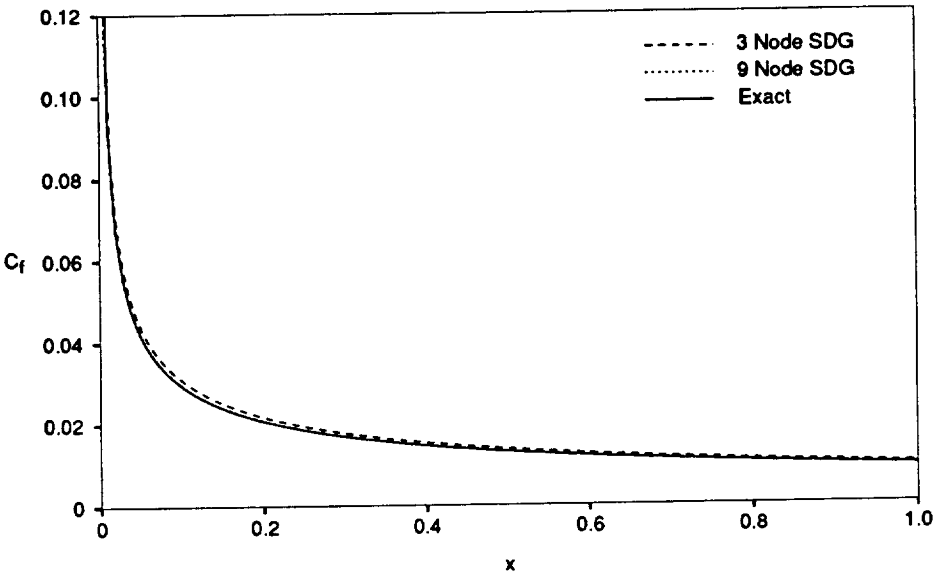

Figure 5.3 3 and 9-Node Comparison of Computed and Exact Skin Friction for a Flat Plate at $M_\infty = 0.800$, $Re = 5000$

all directions. The transpiration velocity boundary condition was used as the VII coupling mechanism and was relaxed after each global VII iteration according to

$$v_{t,rel}^{q} = v_t^q + (1-\omega)v_t^{q-1}, \tag{5.3}$$

where q denotes a particular global VII iteration and ω is a relaxation parameter. The relaxation parameter was set equal to 0.1 for all NACA 0012 calculations. Convergence of the scheme was assumed when lift and total drag coefficients changed less than 0.1% between global iterations. The maximum number of global VII iterations was set at 50, and the ratio of local inviscid to viscous iterations was set at 100. A boundary-layer discretization of 9 nodes was used and the marching routine was controlled in the same manner as the flat-plate calculations by setting $\lambda = 5.0 \times 10^{-4}$.

5.3.1 NACA 0012 - Case A

This test case consists of a NACA 0012 airfoil at a numerical angle of attack of -0.14, a freestream Mach number of 0.499, and a Reynolds number of 9.0×10^6. The flow is attached

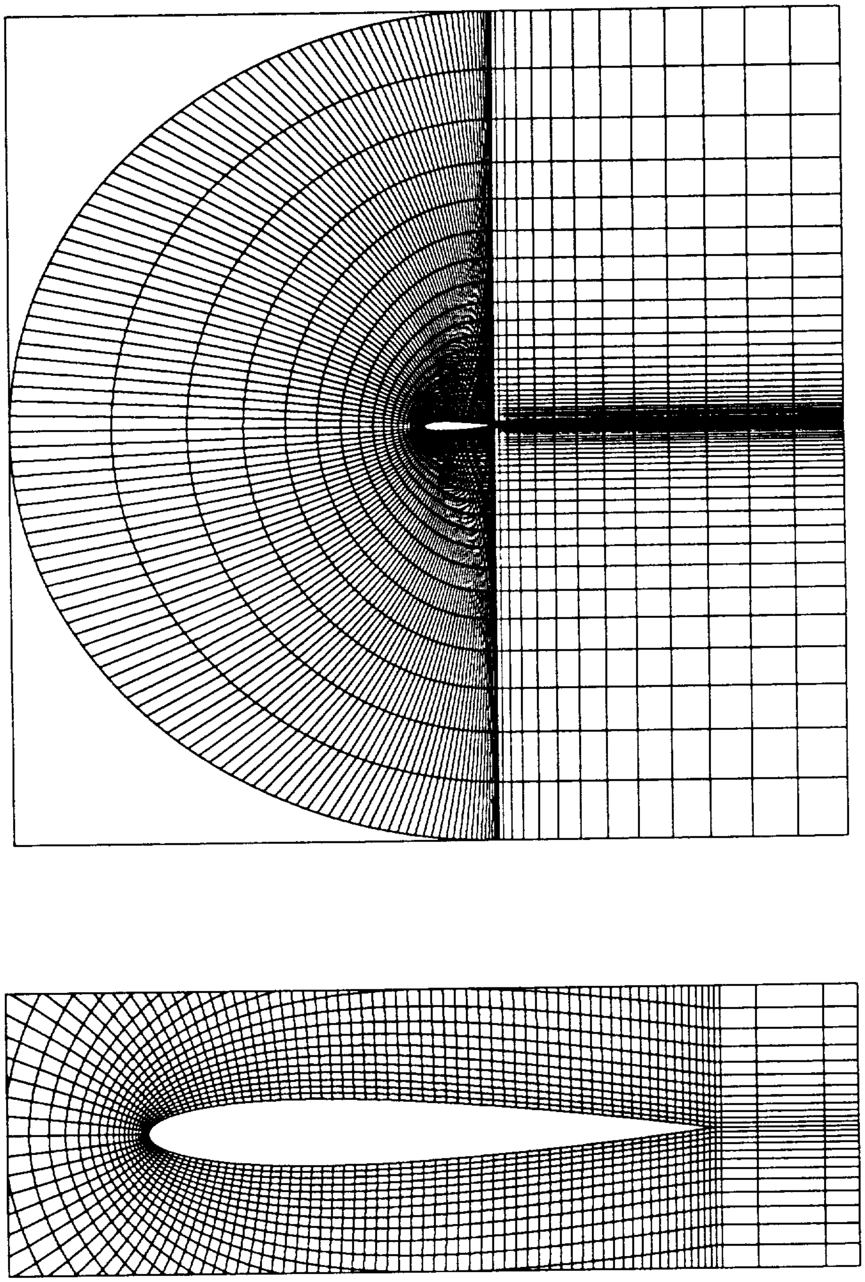

Figure 5.4 NACA 0012 C-Grid used by GAUSS2

Table 5.1 NACA 0012 Test Cases

Case	M_∞	Re	α_{exp}	α_{num}	Ref.
A	0.499	9.0×10^6	-0.14	-0.14	[30]
B	0.700	9.0×10^6	1.86	1.37	[30]

and subsonic over the entire airfoil surface. Transition to turbulence was numerically tripped at the leading edge. The computed coefficient of pressure compares reasonably well with experiment but is slightly underpredicted over the aft section to the trailing edge of the airfoil as shown in Figure 5.5. No experimental data was readily available to compare the computed friction coefficient and displacement thickness, but both C_f and δ^* are plotted in Figures 5.6 and 5.7 for future reference.

5.3.2 NACA 0012 - Case B

This test case consists of a NACA 0012 airfoil at a numerical angle of attack of 1.37, a freestream Mach number of 0.700, and a Reynolds number of 9.0×10^6. For this case, the flow is attached and just slightly supersonic near the leading-edge upper surface. A comparison of experimental and calculated coefficient of pressure is shown in Figure 5.8. The predicted C_p compares well with experiment but slightly overpredicts the peak value at the supersonic region near the leading edge and deviates at the trailing edge. Again, the computed skin friction and displacement thickness values are plotted in Figures 5.9 and 5.10 for future reference.

5.3.3 Aerodynamic Characteristics

Figure 5.11 shows a comparison of lift coefficient vs. angle of attack for the NACA 0012 airfoil at $M_\infty = 0.700$ and $Re = 9.0 \times 10^6$. The SDG VII scheme overpredicts coefficient of lift at low angles of attack, but the prediction improves at higher angles of attack. For angles of attack above 1.54, the flow is more strongly transonic and eventually separates. Drag polar comparisons are displayed in Figure 5.12 for the NACA 0012 airfoil at $M_\infty = 0.700$ and $Re = 9.0 \times 10^6$. The data again shows that the computed lift coefficient is overpredicted at lower angles of attack. It is also noted that the computed drag coefficient

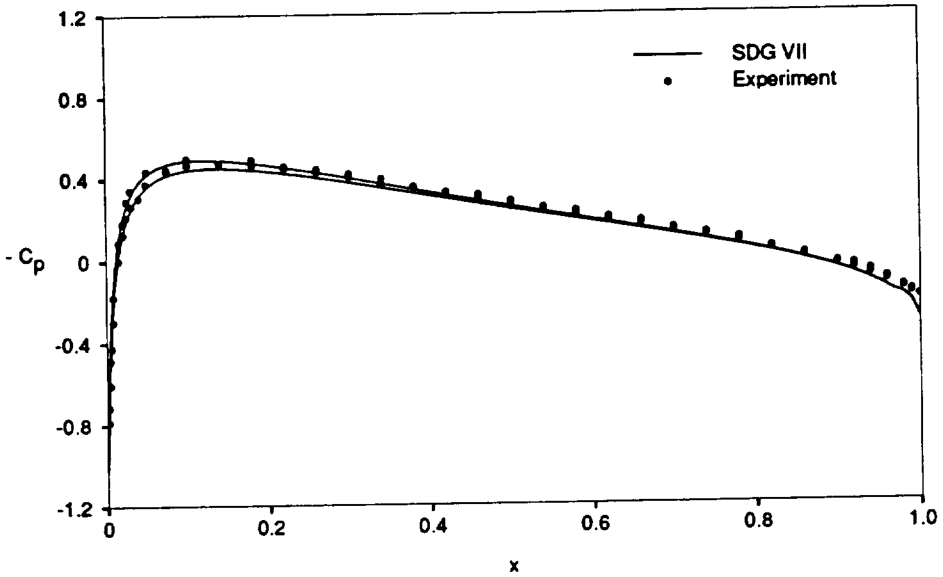

Figure 5.5 Comparison of Pressure Coefficient Distribution for the NACA 0012 Airfoil at $M_\infty = 0.499$, $\alpha_{num} = -0.14$, $Re = 9.0 \times 10^6$

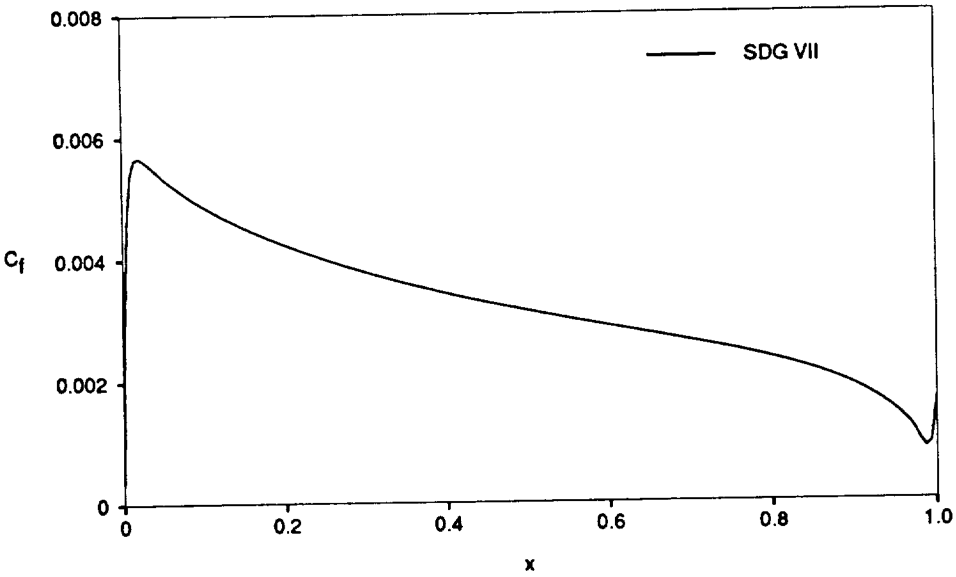

Figure 5.6 Skin Friction Coefficient Distribution for the NACA 0012 Airfoil Upper-Surface at $M_\infty = 0.499$, $\alpha_{num} = -0.14$, $Re = 9.0 \times 10^6$

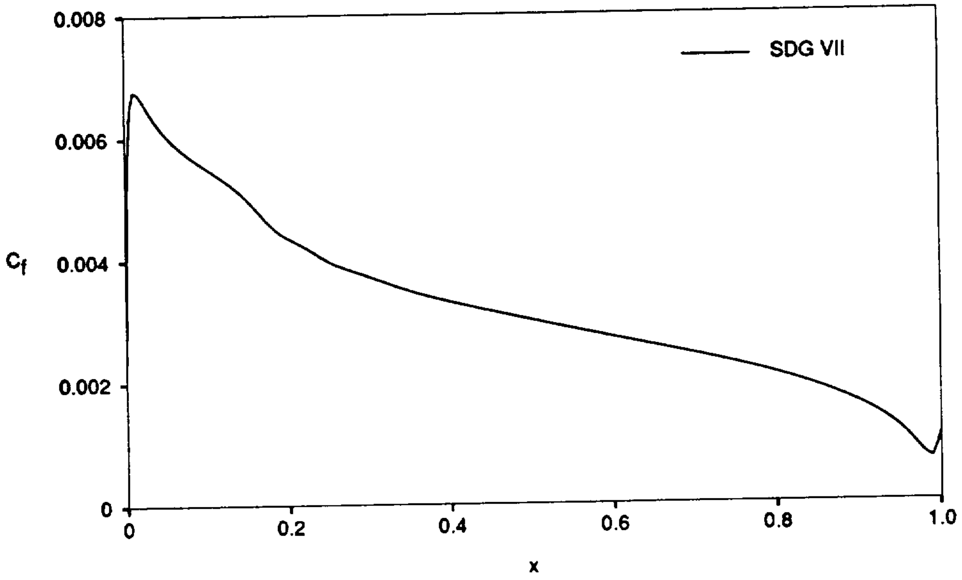

Figure 5.9 Skin Friction Coefficient Distribution for the NACA 0012 Airfoil Upper-Surface at $M_\infty = 0.700$, $\alpha_{num} = 1.37$, $Re = 9.0 \times 10^6$

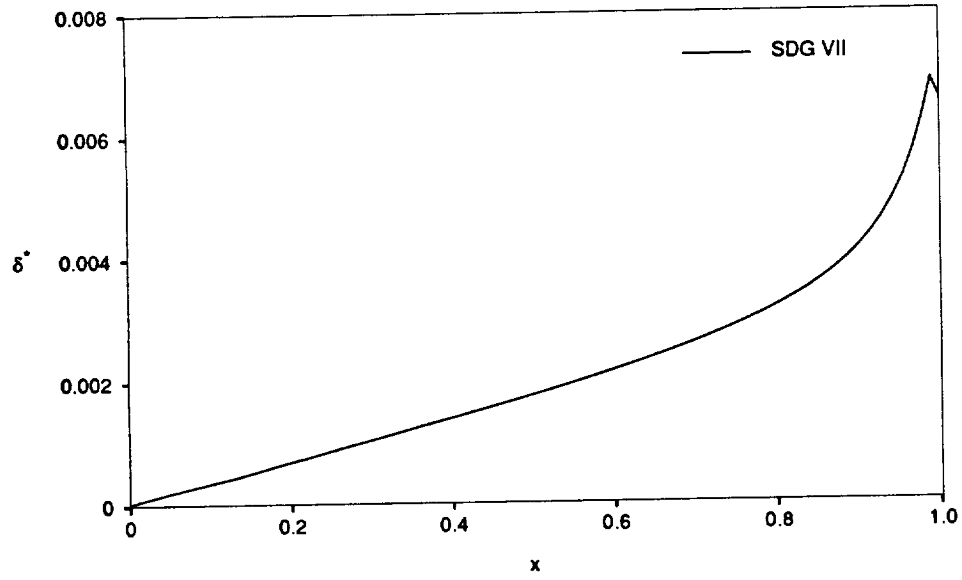

Figure 5.10 Upper-Surface Displacement Thickness for the NACA 0012 Airfoil at $M_\infty = 0.700$, $\alpha_{num} = 1.37$, $Re = 9.0 \times 10^6$

is underpredicted at lower angles of attack with an improved prediction at higher incidence. The flowfield is subsonic for C_L values of approximately 0.2 and lower. Drag values below this point correspond to pressure plus skin friction drag. Drag values above this point have, in addition, a wave drag component. Transonic drag-rise characteristics for the NACA 0012 airfoil at zero-lift conditions are displayed in Figure 5.13. The turbulent boundary layer was numerically tripped at the leading edge, and all computations were performed at a Reynolds number of 9 million. The cross-hatch range of experimental values is based on a "best of six" set of data as described by McCroskey [32]. An underprediction of the drag coefficient is observed at lower Mach numbers with a trend toward improved results at higher Mach numbers.

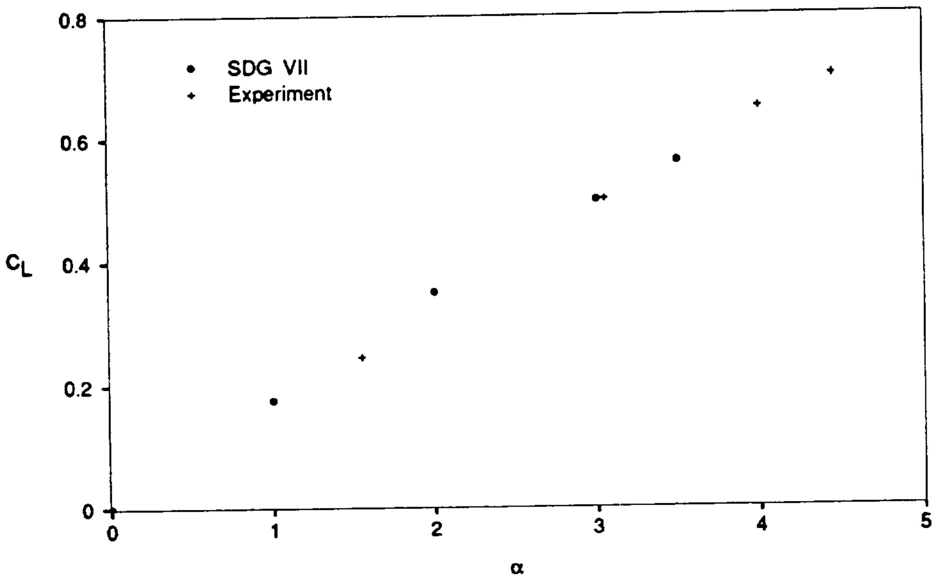

Figure 5.11 Comparison of Lift Coefficient vs. Angle of Attack for the NACA 0012 Airfoil at $M_\infty = 0.700$, $Re = 9.0 \times 10^6$

5.4 RAE 2822 Airfoil

The RAE 2822 was chosen as a supplementary test airfoil for the compressible turbulent VII interaction. The RAE 2822 is a supercritical airfoil with a moderate amount of aft camber which poses a challenge in achieving VII convergence. Also, the experimental

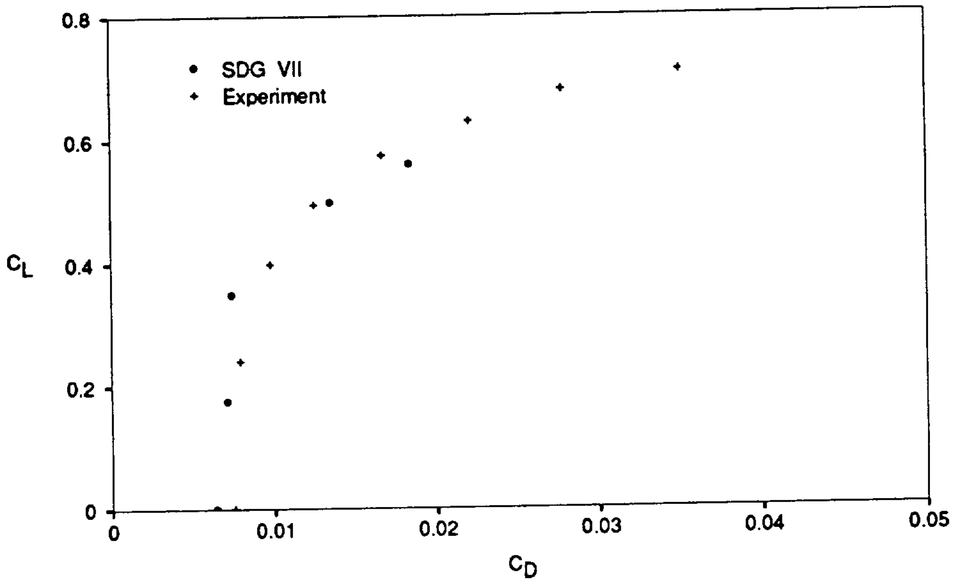

Figure 5.12 Comparison of Lift vs. Drag Polars for the NACA 0012 Airfoil at $M_\infty = 0.700$, $Re = 9.0 \times 10^6$

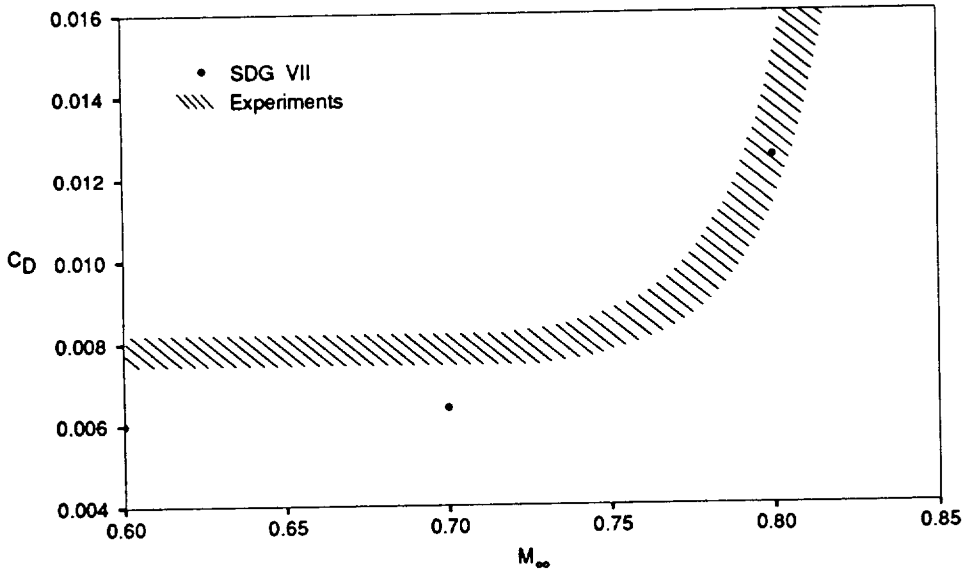

Figure 5.13 Comparison of Computed and Measured Transonic Drag-Rise Characteristics for the NACA 0012 Airfoil at $\alpha_{num} = 0$, $Re = 9.0 \times 10^6$

data in Reference [31] contains a number of boundary-layer and wake parameters such as displacement thickness, momentum thickness, and skin friction which are helpful in validating the boundary-layer solution. The airfoil is tested for attached turbulent flow at high Reynolds numbers and transonic speeds as shown in Table 5.2. A C-grid similar to the one use for the NACA 0012 test cases was used for all of the RAE 2822 calculations. The relaxation parameter was reduced to $\omega = 0.05$ which produced a slower but more stable VII convergence. Consequently, the maximum number of global VII iterations was increased to 75. The discretization and marching-routine controls were set at values equal to those used in the NACA 0012 test cases. For the all of the RAE 2882 cases, the skin friction coefficient is based on the boundary-layer edge dynamic pressure.

Table 5.2 RAE 2822 Test Cases

Case	M_∞	Re	α_{exp}	α_{num}	Ref.
A	0.676	5.7×10^6	-2.18	-2.18	[31]
B	0.676	5.7×10^6	2.40	1.90	[31]
C	0.725	6.5×10^6	2.55	2.10	[31]

5.4.1 RAE 2822 - Case A

This test case consists of a RAE 2822 airfoil at a numerical angle of attack of -2.18, a freestream Mach number of 0.676, and a Reynolds number of 5.7×10^6. The flow in this case is subsonic and attached over the entire airfoil surface. The computed coefficient of pressure shown in Figure 5.14 compares well with the experimental values. The C_p is slightly underpredicted on the lower surface near the leading edge and again deviates from experiment at the trailing edge. The coefficient of friction and displacement thickness results given in Figures 5.15 and 5.16 have good agreement with the experimental values. As seen in Figure 5.15, turbulence was tripped at $x = 0.11$. Figure 5.17 shows the velocity profiles in the boundary layer at three x-locations. The velocity profile deviation from experimental values is attributed to the fact that the SDG method calculates velocity indirectly since shear stress is a dependent variable.

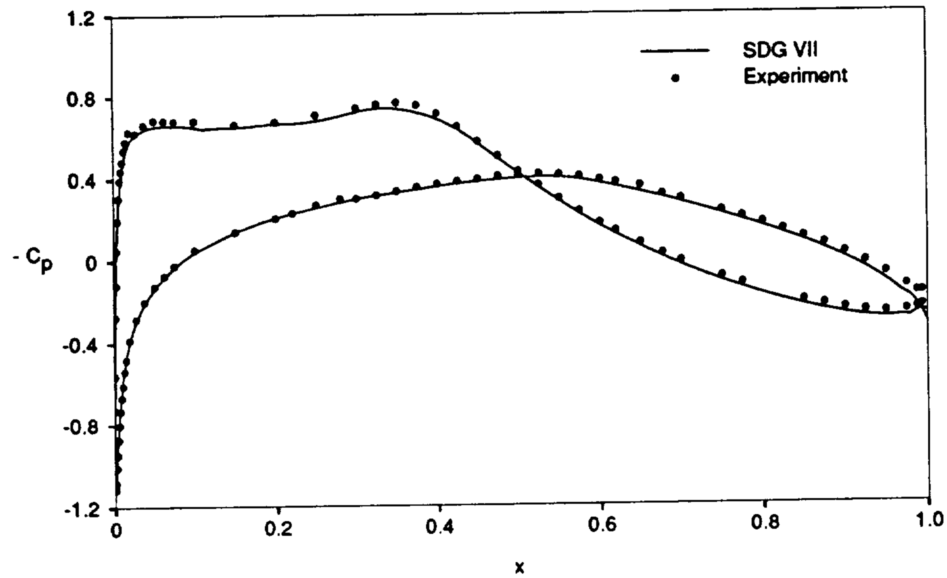

Figure 5.14 Comparison of Pressure Coefficient Distribution for the RAE 2822 Airfoil at $M_\infty = 0.676$, $\alpha_{num} = -2.18$, $Re = 5.7 \times 10^6$

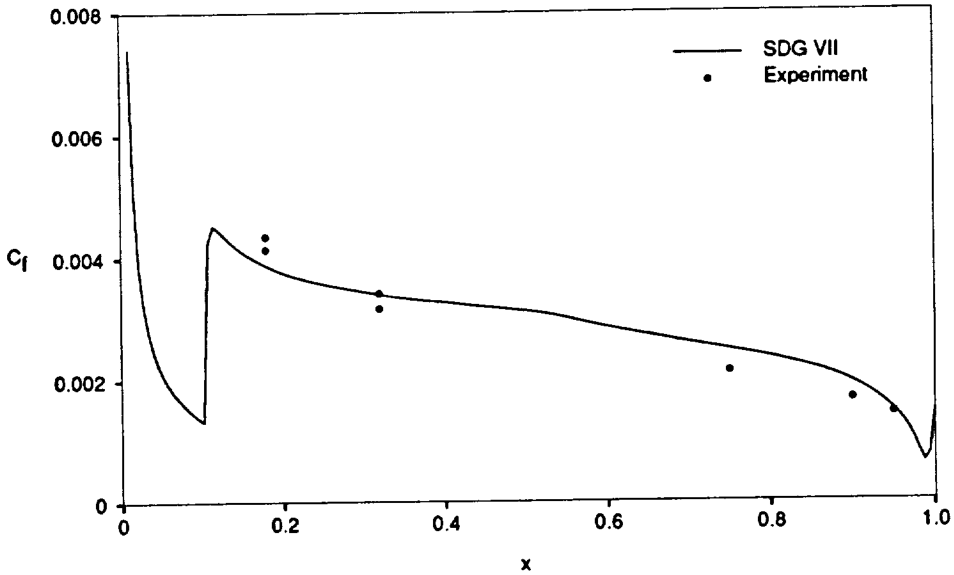

Figure 5.15 Comparison of Upper-Surface Skin Friction Coefficient for the RAE 2822 Airfoil at $M_\infty = 0.676$, $\alpha_{num} = -2.18$, $Re = 5.7 \times 10^6$

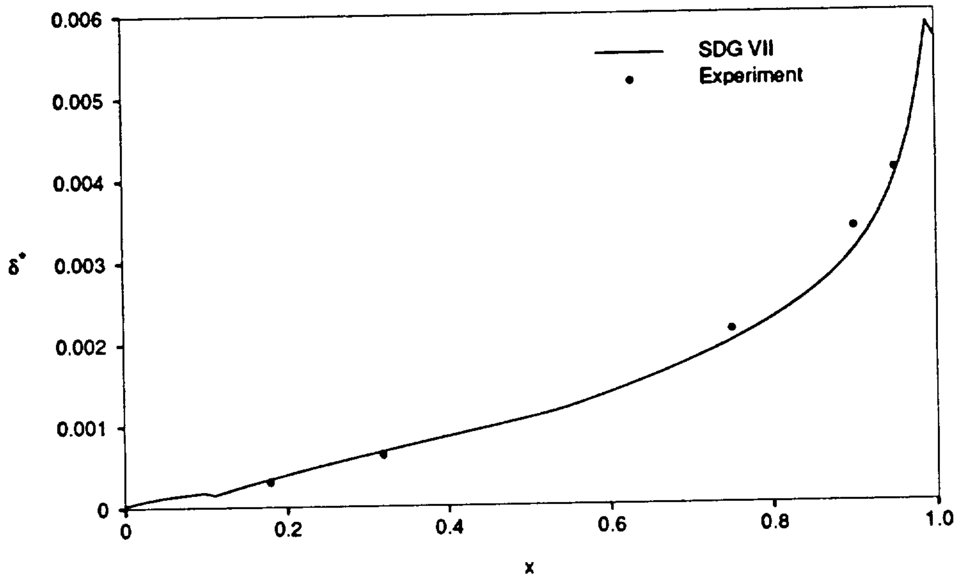

Figure 5.16 Upper-Surface Displacement Thickness Comparison for the RAE 2822 Airfoil at $M_\infty = 0.676$, $\alpha_{num} = -2.18$, $Re = 5.7 \times 10^6$

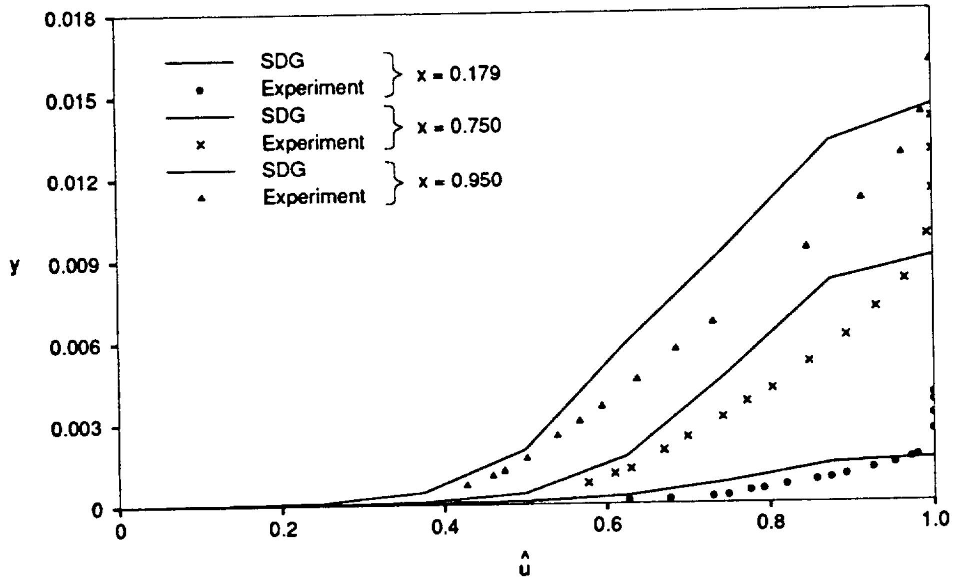

Figure 5.17 Comparison of Computed and Measured Velocity Profiles for the RAE 2822 Airfoil at $M_\infty = 0.676$, $\alpha_{num} = -2.18$, $Re = 5.7 \times 10^6$

5.4.2 RAE 2822 - Case B

This test case consists of a RAE 2822 airfoil at a numerical angle of attack of 1.90, a freestream Mach number of 0.676, and a Reynolds number of 5.7×10^6. The flow is attached over the entire surface and slightly supersonic near the leading edge on the upper surface of the airfoil. Transition to turbulence was numerically tripped at $x = 0.03$. The computed coefficient of pressure is compared with experimental values in Figure 5.18. The C_p prediction on the lower surface of the airfoil is in good agreement with experiment except at the trailing edge, and the upper-surface prediction is slightly below experimental values over the aft section of the airfoil. It should be noted that the pressure coefficient prediction in the supersonic flow region is in good agreement with experiment. Both coefficient of friction and displacement thickness values compare well with the experimental values as shown in Figures 5.19-5.20.

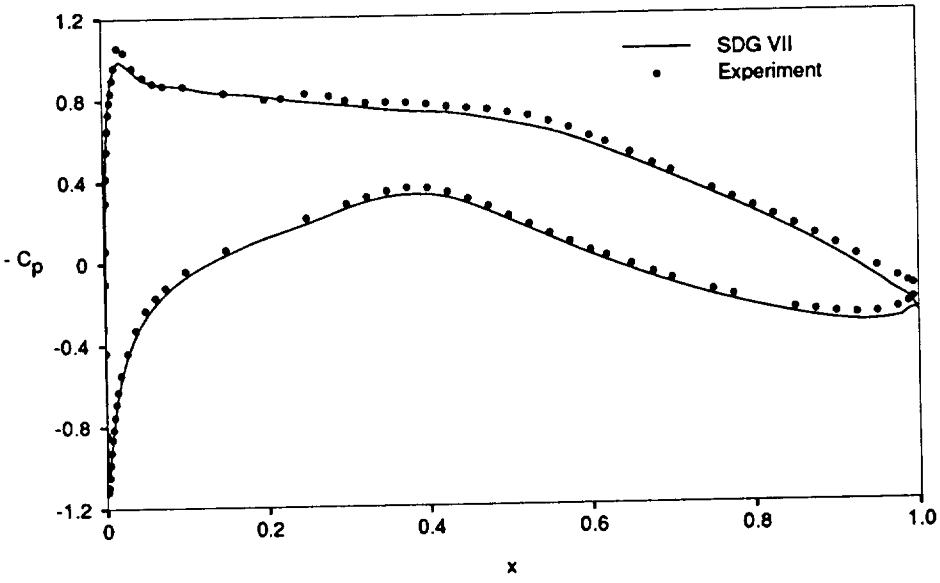

Figure 5.18 Comparison of Pressure Coefficient Distribution for the RAE 2822 Airfoil at $M_\infty = 0.676$, $\alpha_{num} = 1.90$, $Re = 5.7 \times 10^6$

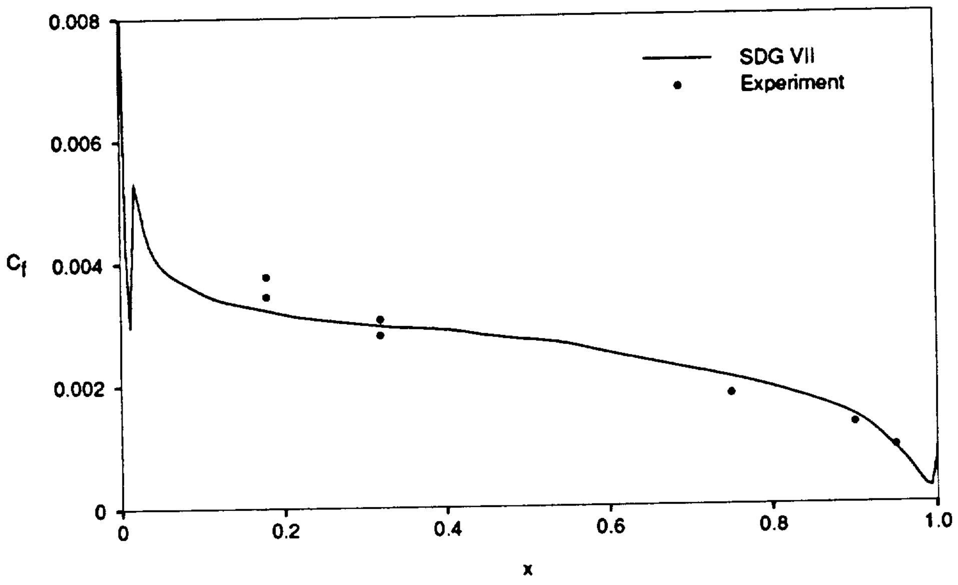

Figure 5.19 Comparison of Upper-Surface Skin Friction Coefficient for the RAE 2822 Airfoil at $M_\infty = 0.676$, $\alpha_{num} = 1.90$, $Re = 5.7 \times 10^6$

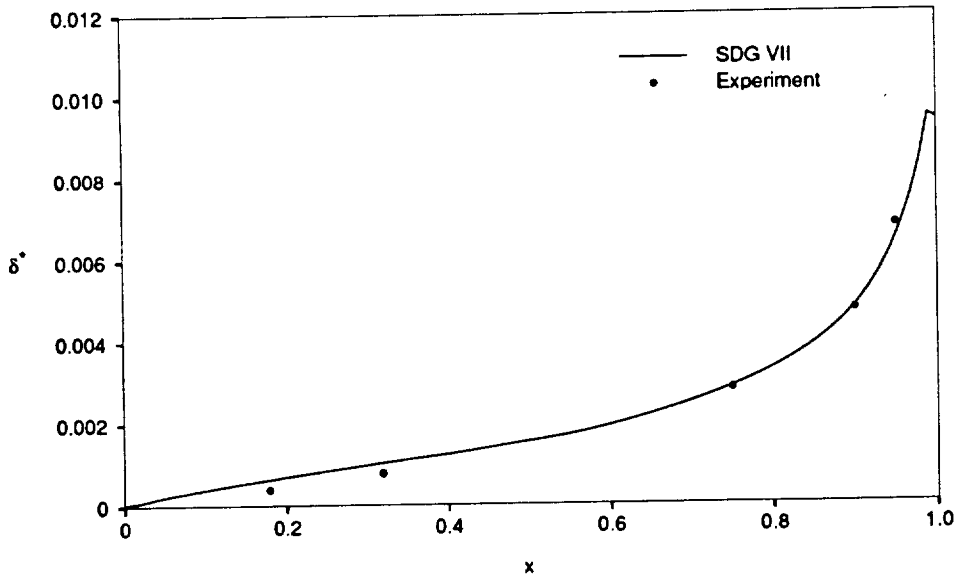

Figure 5.20 Upper-Surface Displacement Thickness Comparison for the RAE 2822 Airfoil at $M_\infty = 0.676$, $\alpha_{num} = 1.90$, $Re = 5.7 \times 10^6$

5.4.3 RAE 2822 - Case C

This test case consists of a RAE 2822 airfoil at a numerical angle of attack of 2.10, a freestream Mach number of 0.725, and a Reynolds number of 6.5×10^6. The transition to turbulence was again numerically tripped at $x = 0.03$. For this case, the flow is attached and supersonic on the upper surface where a moderately strong shock wave is experienced. A comparison of experimental and calculated coefficient of pressure is shown in Figure 5.21. The predicted C_p compares relatively well with experiment except at the shock wave which is predicted upstream of the experimental result. The coefficient of friction and displacement thickness results given in Figures 5.22 and 5.23 have good agreement with the experimental values.

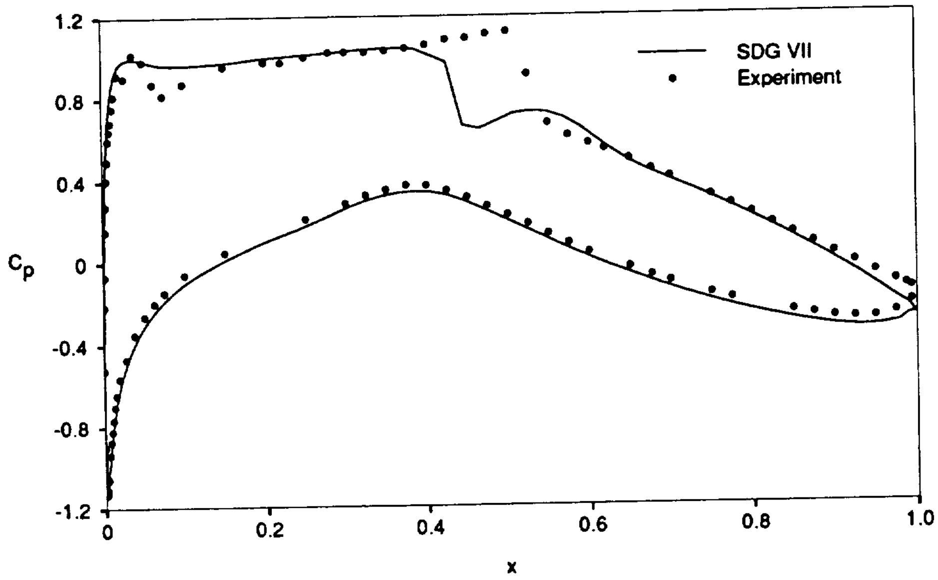

Figure 5.21 Comparison of Pressure Coefficient Distribution for the RAE 2822 Airfoil at $M_\infty = 0.725$, $\alpha_{num} = 2.10$, $Re = 6.5 \times 10^6$

5.5 Grid Refinement Study

A grid refinement study was performed to demonstrate the sensitivity of computed force coefficients to the grid spacing used in the SDG VII scheme. The NACA 0012 airfoil

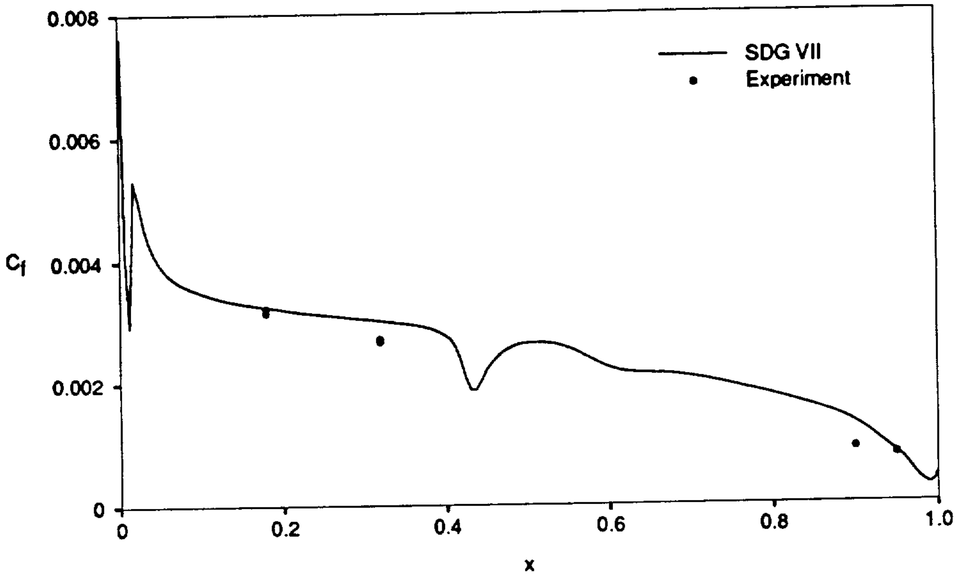

Figure 5.22 Comparison of Upper-Surface Skin Friction Coefficient for the RAE 2822 Airfoil at $M_\infty = 0.725$, $\alpha_{num} = 2.10$, $Re = 6.5 \times 10^6$

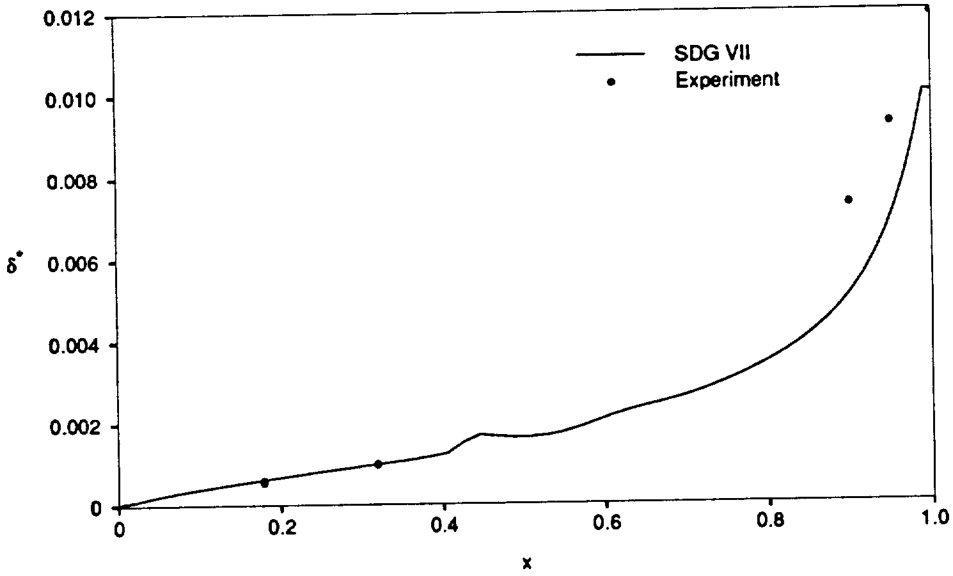

Figure 5.23 Upper-Surface Displacement Thickness Comparison for the RAE 2822 Airfoil at $M_\infty = 0.725$, $\alpha_{num} = 2.10$, $Re = 6.5 \times 10^6$

was solved at flow conditions given in Case A for a number of viscous finite element discretizations and inviscid grid sizes. Figure 5.24 is a plot of computed lift coefficient vs. finite element space width for coarse (81 × 17) and fine (161 × 33) inviscid grids. The trend is to decrease the lift coefficient with increasing space width. The effect of grid spacing on the computed drag coefficient is shown in Figure 5.25, where the trend is to increase the drag coefficient with increasing space width. The relatively small slope of each curve indicates the method produces reasonable drag levels on coarse grids, which is a highly-desirable characteristic of any computational method.

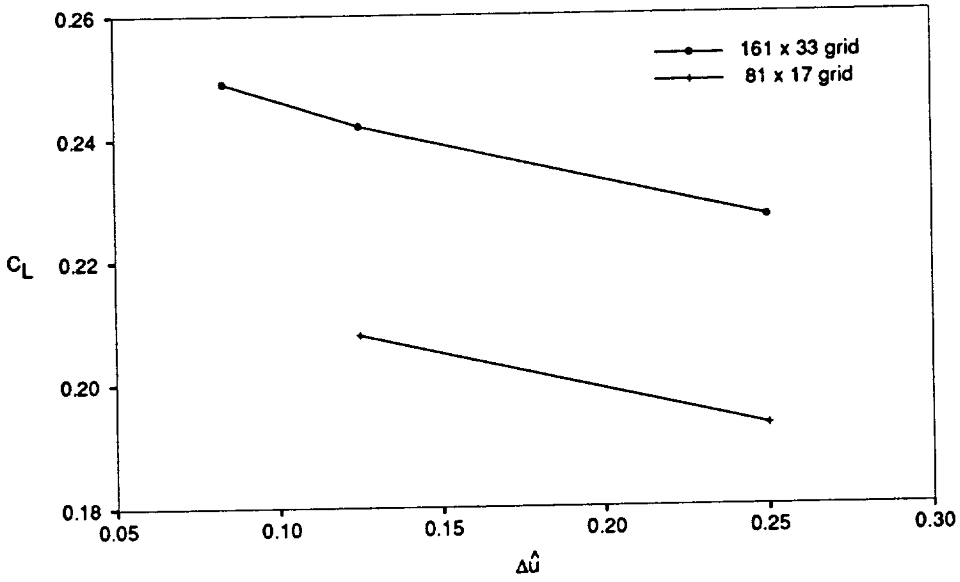

Figure 5.24 Comparison of Lift Coefficient vs. Boundary-Layer Space Width for the NACA 0012 Airfoil - Case A

5.6 Aerodynamic Force Coefficients

A summary of computed lift and drag coefficients for the SDG VII method is displayed in Table 5.3. All drag coefficient values are in terms of drag counts where $C_D = 1$ count is equivalent to $C_D = 0.0001$. Since the numerical angle of attack was varied in each case to match computed lift and experimental normal force coefficients, it is important to note that α_{num} was within the accepted corrected angle of attack range for wind tunnel

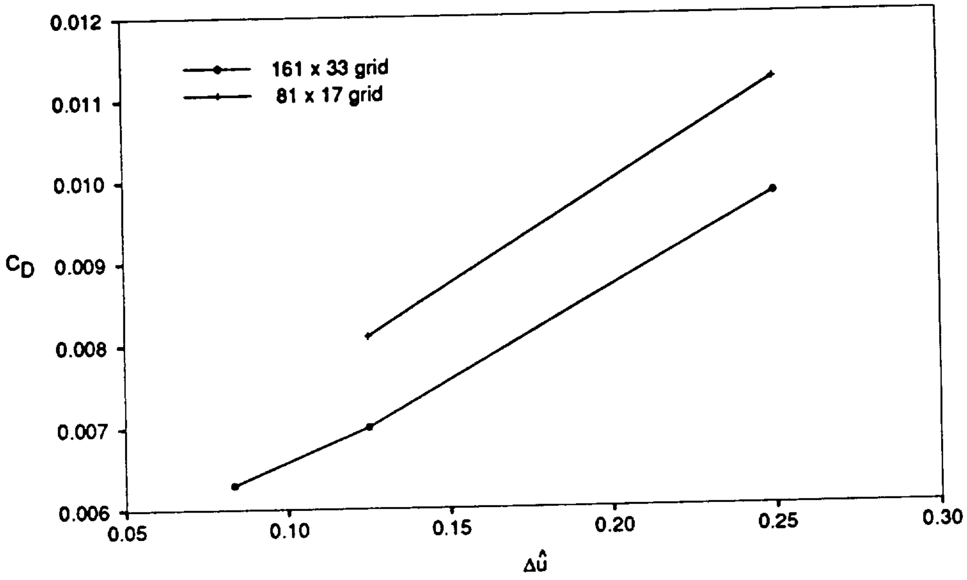

Figure 5.25 Comparison of Drag Coefficient vs. Average Grid Spacing for the NACA 0012 Airfoil - Case A

wall-interference effects [33]. The computed coefficient of drag results for the SDG VII scheme were on average predicted approximately 15% lower than experimentally obtained results. The underprediction of drag is more pronounced at lower angle of attack cases. The current state-of-the-art capabilities for attached flow lift and drag predictions are ±3% range for lift and ±5% range for drag [33].

Table 5.3 Force Coefficient Comparison

NACA 0012 Case	Numerical				Experimental	
	C_L	C_D	C_{Dp}	C_{Dv}	C_L	C_D
A	-0.019	58	-7	65	-0.013	77
B	0.242	70	7	63	0.241	79

RAE 2822 Case	Numerical				Experimental	
	C_L	C_D	C_{Dp}	C_{Dv}	C_L	C_D
A	-0.121	70	7	63	-0.115	79
B	0.565	75	8	67	0.566	85
C	0.658	86	21	65	0.658	107

Chapter 6

Conclusions

The application of the Dorodnitysn transformations to the boundary-layer equations provides a spatial coordinate which automatically follows boundary-layer growth and gives high resolution near the wall which is important in turbulent flows where near-wall velocity gradients are large. The transformed spatial domain is effectively modelled with finite elements to provide accurate results on coarse grids. Modelling the group terms for viscosity by the group finite element method leads to an important economy in the formulation since μ_t need only be evaluated at the nodes. The use of a non-iterative streamwise marching routine also adds computational economy to the method. The resulting boundary layer code can be used to solve any smoothly-connected airfoil shape without modification and is easily coupled with existing inviscid flow solvers. The transpiration velocity approach used to couple the particularly fast and accurate Euler solver used in this analysis serves as a computationally efficient and easily implemented VII coupling mechanism. Convergence of the overall interaction procedure for both the NACA 0012 and RAE 2822 airfoils was achieved in relatively few global iterations while achieving results of adequate engineering accuracy.

Future work with the SDG method should include the use of a maximum reversed flow velocity concept in order to successfully model separation while still retaining a finite spatial grid. Also, the marching routine could be further improved by possibly using a trigonometric streamwise coordinate transformation to smooth external velocity gradients at the leading and trailing edges of the airfoil.

Appendix A

Galerkin Integrals

$$\begin{aligned} K1_{ji} &= \int_{\hat{u}_{j-1}}^{\hat{u}_j} \hat{u} N_j N_{j-1} d\hat{u} \\ &+ \int_{\hat{u}_{j-1}}^{\hat{u}_j} \hat{u} N_j N_j d\hat{u} \\ &+ \int_{\hat{u}_j}^{\hat{u}_{j+1}} \hat{u} N_j N_j d\hat{u} \\ &+ \int_{\hat{u}_j}^{\hat{u}_{j+1}} \hat{u} N_j N_{j+1} d\hat{u} \end{aligned} \tag{A.1}$$

$$\begin{aligned} K2_{ji} &= \int_{\hat{u}_{j-1}}^{\hat{u}_j} \left[(1-\hat{u})\frac{dN_j}{d\hat{u}} - N_j\right] \left[(1-\hat{u})\frac{dN_{j-1}}{d\hat{u}} - N_{j-1}\right] d\hat{u} \\ &+ \int_{\hat{u}_{j-1}}^{\hat{u}_j} \left[(1-\hat{u})\frac{dN_j}{d\hat{u}} - N_j\right] \left[(1-\hat{u})\frac{dN_j}{d\hat{u}} - N_j\right] d\hat{u} \\ &+ \int_{\hat{u}_j}^{\hat{u}_{j+1}} \left[(1-\hat{u})\frac{dN_j}{d\hat{u}} - N_j\right] \left[(1-\hat{u})\frac{dN_j}{d\hat{u}} - N_j\right] d\hat{u} \\ &+ \int_{\hat{u}_j}^{\hat{u}_{j+1}} \left[(1-\hat{u})\frac{dN_j}{d\hat{u}} - N_j\right] \left[(1-\hat{u})\frac{dN_{j+1}}{d\hat{u}} - N_{j+1}\right] d\hat{u} \end{aligned} \tag{A.2}$$

$$\begin{aligned} K3_{ji} &= \int_{\hat{u}_{j-1}}^{\hat{u}_j} (1+\hat{u}) \left[(1-\hat{u})\frac{dN_j}{d\hat{u}} - N_j\right] N_{j-1} d\hat{u} \\ &+ \int_{\hat{u}_{j-1}}^{\hat{u}_j} (1+\hat{u}) \left[(1-\hat{u})\frac{dN_j}{d\hat{u}} - N_j\right] N_j \\ &+ \int_{\hat{u}_j}^{\hat{u}_{j+1}} (1+\hat{u}) \left[(1-\hat{u})\frac{dN_j}{d\hat{u}} - N_j\right] N_j d\hat{u} \\ &+ \int_{\hat{u}_j}^{\hat{u}_{j+1}} (1+\hat{u}) \left[(1-\hat{u})\frac{dN_j}{d\hat{u}} - N_j\right] N_{j+1} d\hat{u} \end{aligned} \tag{A.3}$$

$$
\begin{aligned}
K4_{ji} &= \int_{\hat{u}_{j-1}}^{\hat{u}_j} \hat{u}(1-\hat{u})N_jN_{j-1}d\hat{u} \\
&+ \int_{\hat{u}_{j-1}}^{\hat{u}_j} \hat{u}(1-\hat{u})N_jN_jd\hat{u} \\
&+ \int_{\hat{u}_j}^{\hat{u}_{j+1}} \hat{u}(1-\hat{u})N_jN_jd\hat{u} \\
&+ \int_{\hat{u}_j}^{\hat{u}_{j+1}} \hat{u}(1-\hat{u})N_jN_{j+1}d\hat{u}
\end{aligned}
\tag{A.4}
$$

$$
\begin{aligned}
K5_{ji} &= \int_{\hat{u}_{j-1}}^{\hat{u}_j} (1-\hat{u}^2)\left[(1-\hat{u})\frac{dN_j}{d\hat{u}} - N_j\right] N_{j-1}d\hat{u} \\
&+ \int_{\hat{u}_{j-1}}^{\hat{u}_j} (1-\hat{u}^2)\left[(1-\hat{u})\frac{dN_j}{d\hat{u}} - N_j\right] N_jd\hat{u} \\
&+ \int_{\hat{u}_j}^{\hat{u}_{j+1}} (1-\hat{u}^2)\left[(1-\hat{u})\frac{dN_j}{d\hat{u}} - N_j\right] N_jd\hat{u} \\
&+ \int_{\hat{u}_j}^{\hat{u}_{j+1}} (1-\hat{u}^2)\left[(1-\hat{u})\frac{dN_j}{d\hat{u}} - N_j\right] N_{j+1}d\hat{u}
\end{aligned}
\tag{A.5}
$$

$$
\begin{aligned}
K6_{ji} &= \int_{\hat{u}_{j-1}}^{\hat{u}_j} (1-\hat{u})^2N_jN_{j-1}d\hat{u} \\
&+ \int_{\hat{u}_{j-1}}^{\hat{u}_j} (1-\hat{u})^2N_jN_jd\hat{u} \\
&+ \int_{\hat{u}_j}^{\hat{u}_{j+1}} (1-\hat{u})^2N_jN_jd\hat{u} \\
&+ \int_{\hat{u}_j}^{\hat{u}_{j+1}} (1-\hat{u})^2N_jN_{j+1}d\hat{u}
\end{aligned}
\tag{A.6}
$$

$$
\begin{aligned}
K7_{ji} &= \int_{\hat{u}_{j-1}}^{\hat{u}_j} \hat{u}(1-\hat{u})N_j\left[(1-\hat{u})\frac{dN_{j-1}}{d\hat{u}} - N_{j-1}\right] d\hat{u} \\
&+ \int_{\hat{u}_{j-1}}^{\hat{u}_j} \hat{u}(1-\hat{u})N_j\left[(1-\hat{u})\frac{dN_j}{d\hat{u}} - N_j\right] d\hat{u} \\
&+ \int_{\hat{u}_j}^{\hat{u}_{j+1}} \hat{u}(1-\hat{u})N_j\left[(1-\hat{u})\frac{dN_j}{d\hat{u}} - N_j\right] d\hat{u} \\
&+ \int_{\hat{u}_j}^{\hat{u}_{j+1}} \hat{u}(1-\hat{u})N_j\left[(1-\hat{u})\frac{dN_{j+1}}{d\hat{u}} - N_{j+1}\right] d\hat{u}
\end{aligned}
\tag{A.7}
$$

$$
\begin{aligned}
K8_{jik} = & \int_{\hat{u}_{j-1}}^{\hat{u}_j} (1-\hat{u}) \left[(1-\hat{u})\frac{dN_j}{d\hat{u}} - N_j\right] \left[(1-\hat{u})\frac{dN_{j-1}}{d\hat{u}} - N_{j-1}\right] N_{j-1} d\hat{u} \\
+ & \int_{\hat{u}_{j-1}}^{\hat{u}_j} (1-\hat{u}) \left[(1-\hat{u})\frac{dN_j}{d\hat{u}} - N_j\right] \left[(1-\hat{u})\frac{dN_j}{d\hat{u}} - N_j\right] N_{j-1} d\hat{u} \\
+ & \int_{\hat{u}_{j-1}}^{\hat{u}_j} (1-\hat{u}) \left[(1-\hat{u})\frac{dN_j}{d\hat{u}} - N_j\right] \left[(1-\hat{u})\frac{dN_{j-1}}{d\hat{u}} - N_{j-1}\right] N_j d\hat{u} \\
+ & \int_{\hat{u}_{j-1}}^{\hat{u}_j} (1-\hat{u}) \left[(1-\hat{u})\frac{dN_j}{d\hat{u}} - N_j\right] \left[(1-\hat{u})\frac{dN_j}{d\hat{u}} - N_j\right] N_j d\hat{u} \\
+ & \int_{\hat{u}_j}^{\hat{u}_{j+1}} (1-\hat{u}) \left[(1-\hat{u})\frac{dN_j}{d\hat{u}} - N_j\right] \left[(1-\hat{u})\frac{dN_j}{d\hat{u}} - N_j\right] N_j d\hat{u} \\
+ & \int_{\hat{u}_j}^{\hat{u}_{j+1}} (1-\hat{u}) \left[(1-\hat{u})\frac{dN_j}{d\hat{u}} - N_j\right] \left[(1-\hat{u})\frac{dN_{j+1}}{d\hat{u}} - N_{j+1}\right] N_j d\hat{u} \\
+ & \int_{\hat{u}_j}^{\hat{u}_{j+1}} (1-\hat{u}) \left[(1-\hat{u})\frac{dN_j}{d\hat{u}} - N_j\right] \left[(1-\hat{u})\frac{dN_j}{d\hat{u}} - N_j\right] N_{j+1} d\hat{u} \\
+ & \int_{\hat{u}_j}^{\hat{u}_{j+1}} (1-\hat{u}) \left[(1-\hat{u})\frac{dN_j}{d\hat{u}} - N_j\right] \left[(1-\hat{u})\frac{dN_{j+1}}{d\hat{u}} - N_{j+1}\right] N_{j+1} d\hat{u}
\end{aligned}
\tag{A.8}
$$

$$
\begin{aligned}
K9_{jik} = & \int_{\hat{u}_{j-1}}^{\hat{u}_j} (1-\hat{u}) \left[(1-\hat{u})\frac{dN_j}{d\hat{u}} - N_j\right] N_{j-1} \left[(1-\hat{u})\frac{dN_{j-1}}{d\hat{u}} - N_{j-1}\right] d\hat{u} \\
+ & \int_{\hat{u}_{j-1}}^{\hat{u}_j} (1-\hat{u}) \left[(1-\hat{u})\frac{dN_j}{d\hat{u}} - N_j\right] N_j \left[(1-\hat{u})\frac{dN_{j-1}}{d\hat{u}} - N_{j-1}\right] d\hat{u} \\
+ & \int_{\hat{u}_{j-1}}^{\hat{u}_j} (1-\hat{u}) \left[(1-\hat{u})\frac{dN_j}{d\hat{u}} - N_j\right] N_{j-1} \left[(1-\hat{u})\frac{dN_j}{d\hat{u}} - N_j\right] d\hat{u} \\
+ & \int_{\hat{u}_{j-1}}^{\hat{u}_j} (1-\hat{u}) \left[(1-\hat{u})\frac{dN_j}{d\hat{u}} - N_j\right] N_j \left[(1-\hat{u})\frac{dN_j}{d\hat{u}} - N_j\right] d\hat{u} \\
+ & \int_{\hat{u}_j}^{\hat{u}_{j+1}} (1-\hat{u}) \left[(1-\hat{u})\frac{dN_j}{d\hat{u}} - N_j\right] N_j \left[(1-\hat{u})\frac{dN_j}{d\hat{u}} - N_j\right] d\hat{u} \\
+ & \int_{\hat{u}_j}^{\hat{u}_{j+1}} (1-\hat{u}) \left[(1-\hat{u})\frac{dN_j}{d\hat{u}} - N_j\right] N_{j+1} \left[(1-\hat{u})\frac{dN_j}{d\hat{u}} - N_j\right] d\hat{u} \\
+ & \int_{\hat{u}_j}^{\hat{u}_{j+1}} (1-\hat{u}) \left[(1-\hat{u})\frac{dN_j}{d\hat{u}} - N_j\right] N_j \left[(1-\hat{u})\frac{dN_{j+1}}{d\hat{u}} - N_{j+1}\right] d\hat{u} \\
+ & \int_{\hat{u}_j}^{\hat{u}_{j+1}} (1-\hat{u}) \left[(1-\hat{u})\frac{dN_j}{d\hat{u}} - N_j\right] N_{j+1} \left[(1-\hat{u})\frac{dN_{j+1}}{d\hat{u}} - N_{j+1}\right] d\hat{u}
\end{aligned}
\tag{A.9}
$$

$$
\begin{aligned}
K10_{jik} &= N_j N_{j-1}\left[(1-\hat{u})\frac{dN_{j-1}}{d\hat{u}} - N_{j-1}\right] d\hat{u} \\
&+ N_j N_j\left[(1-\hat{u})\frac{dN_{j-1}}{d\hat{u}} - N_{j-1}\right] d\hat{u} \\
&+ N_j N_{j-1}\left[(1-\hat{u})\frac{dN_{j}}{d\hat{u}} - N_{j}\right] d\hat{u} \\
&+ N_j N_j\left[(1-\hat{u})\frac{dN_{j}}{d\hat{u}} - N_{j}\right] d\hat{u} \\
&+ N_j N_j\left[(1-\hat{u})\frac{dN_{j}}{d\hat{u}} - N_{j}\right] d\hat{u} \\
&+ N_j N_{j+1}\left[(1-\hat{u})\frac{dN_{j}}{d\hat{u}} - N_{j}\right] d\hat{u} \\
&+ N_j N_j\left[(1-\hat{u})\frac{dN_{j+1}}{d\hat{u}} - N_{j+1}\right] d\hat{u} \\
&+ N_j N_{j+1}\left[(1-\hat{u})\frac{dN_{j+1}}{d\hat{u}} - N_{j+1}\right] d\hat{u}
\end{aligned}
\tag{A.10}
$$

Bibliography

[1] F.G. Blottner, "Computational Techniques for Boundary Layers," AGARD-LN-73, 1975.

[2] M. Holt and T.A. Lu, "Supersonic Laminar Boundary Layer Separation in a Concave Corner," *Acta Astronautica*, **2**, pp. 409-429, 1975.

[3] C.A.J. Fletcher, "A Dorodnitsyn Finite Element Formulation for Turbulent Boundary Layers," *Computers and Fluids*, **12**, pp. 31-45, 1983.

[4] S.L. Strong, "A Numerical Study of Laminar, Compressible Boundary Layer About an Airfoil," Masters Thesis, Rice University, 1991.

[5] L. Prandtl, "The Mechanics of Viscous Fluids," *Aerodynamic Theory Vol. 3*, Springer, Berlin, 1935.

[6] J.E. Green, D.J. Weeks, and J.W.F. Brooman "Prediction of Turbulent Boundary Layers and Wakes in Incompressible Flow by a Lag-Entrainment Method," British Aeronautical Research Council Reports and Memoranda No. 3791, 1977.

[7] M.R. Collyer and R.C. Lock, "Prediction of Viscous Effects in Steady Transonic Flow Past an Aerofoil," *Aeronautical Quarterly*, **30**, pp. 485, 1977.

[8] R.E. Melnik, R. Chow, H.R. Mead, and Jameson, "Theory of Viscous Transonic Flow Over Airfoils at High Reynolds Number," *AIAA Paper 77-680*, 1977.

[9] T. Cebeci and A.M.O. Smith, *Analysis of Turbulent Boundary Layers*, Academic Press, 1984.

[10] K.H. Huebner and E.A. Thornton, *The Finite Element Method for Engineers*, John Wiley and Sons, New York, 1982.

[11] C.A.J. Fletcher, *Computational Galerkin Methods*, Springer-Verlag, New York, 1984.

[12] C.A.J. Fletcher, "The Group Finite Element Formulation," *Computer Methods in Applied Mechanics and Engineering*, **37**, pp. 225-243, 1983.

[13] S.D. Conte and C. DeBoor, *Elementary Numerical Analysis, an Algorithmic Approach*, McGraw-Hill, 1972.

[14] L. Prandtl, "Motions of Fluids with Very Little Viscosity," *NACA TM-452*, 1928.

[15] A.A. Dorodnitsyn, "General Method of Integral Relations and it's Application to Boundary Layer Theory," *Advanced Aeronautical Science*, **3**, pp. 207-219, 1962.

[16] D.R. Chapman and M.W. Rubesin, "Temperature and Velocity Profiles in the Compressible Laminar Boundary Layer with Arbitrary Distribution of Surface Temperature," *Journal of Aeronautical Science*, **16**, pp. 547-565, 1949.

[17] A.J. Meade, Jr., "Semi-Discrete Galerkin Modelling of Compressible Viscous Flow Past a Circular Cone at Incidence," Ph.D Thesis, University of California, Berkeley, 1989.

[18] C.A.J. Fletcher, "A Dorodnitsyn Finite Element Formulation for Laminar Boundary Layer Flow," *International Journal for Numerical Methods in Fluids*, **4**, pp. 399-419, 1984.

[19] W.R. Briley and H. MacDonald, "Solution of the Multidimensional Compressible N-S Equations by a General Implicit Method," *Journal of Computational Physics*, **24**, pp. 372-397, 1977.

[20] F. White, *Viscous Fluid Flow*, McGraw-Hill, 1974.

[21] H. Schlicting, *Boundary-Layer Theory*, McGraw-Hill, 1987.

[22] B.S. Baldwin and H. Lomax, "Thin Layer Approximation and Algebraic Model for Separated Turbulent Flow," *AIAA Paper 78-257*, 1978.

[23] P.S. Granville, "Baldwin-Lomax Factors for Turbulent Boundary Layers in Pressure Gradients," *AIAA Journal*, **25**, pp. 1624-1627, 1979.

[24] M.J. Lighthill, "On Displacement Thickness," *Journal of Fluid Mechanics*, **4**, pp. 383-392, 1958.

[25] V.N. Vatsa and J.M. Verdon, "Viscid/Inviscid Interaction Analysis of Separated Trailing Edge Flows," *AIAA Journal*, **23**, pp. 281-489, 1985.

[26] W.R. Van Dalsem, J.L. Steger, and K.V. Rao, "Some Experiences with the Viscous-Inviscid Interaction Approach," *NASA TM 100015*, pp. 1987.

[27] J.C. Le Balleur, "Numerical Flow Calculation and Viscous-Inviscid Interaction Techniques," *Computation Methods in Viscous Flows Vol. 3*, pp. 419-450, Pineridge Press, 1984.

[28] P.M. Hartwich, "Fresh Look at Shock Fitting," *AIAA Paper 90-0108*, 1990.

[29] P.M. Hartwich, "Split Coefficient Matrix (SCM) Method with Floating Shock Fitting for Transonic Airfoils," *Proceeding of the 12th International Conference on Numerical Methods in Fluid Dynamics*, Lecture Notes in Physics, Springer-Verlag, New York, 1991.

[30] C.D. Harris, "Two-Dimensional Aerodynamic Characteristics of the NACA 0012 Airfoil in the Langley 8-Foot Transonic Pressure Tunnel," NASA TM-81927, 1981.

[31] P.H. Cook, M.A. McDonald, and M.C.P. Firmin, "Aerofoil RAE2822 - Pressure Distributions, and Boundary Layer and Wake Measurements," AGARD-AR-138, 1979

[32] W.J. McCroskey, "A Critical Assessment of Wind Tunnel Results for the NACA 0012 Airfoil," Paper 1, AGARD Fluid Dynamics Panel Symposium on Aerodynamic Data Accuracy and Quality: Requirements and Capabilities in Wind Tunnel Testing, Naples, Italy, 1987.

[33] T.L. Holst, "Viscous Transonic Airfoil Workshop Compendium of Results," *Journal of Aircraft*, **25**, pp. 1073-1087, 1988.

User Manual for SDG VII Airfoil Analysis Codes

Introduction

A method is developed for solution of the two-dimensional, steady, compressible, turbulent boundary-layer equations and is coupled to an existing Euler solver for attached transonic airfoil analysis problems. The boundary-layer formulation utilizes the semi-discrete Galerkin (SDG) method to model the spatial variables with linear finite elements and the time-like variables with finite differences. A Dorodnitsyn transformed system of equations is used to replace the infinite spatial domain with a finite domain thereby permitting the use of a uniform finite element grid which provides high resolution near the wall and automatically follows boundary-layer growth. The second-order accurate Crank-Nicholson scheme is applied along with a linearization method to take advantage of the parabolic nature of the boundary-layer equations and generate a non-iterative marching routine. The SDG code can be applied to any smoothly-connected airfoil shape without modification and can be coupled to any inviscid flow solver. A direct viscous-inviscid interaction is accomplished between the Euler (GAUSS2) and boundary-layer (SDGM) codes through the application of a transpiration velocity boundary condition. Gross effects of turbulence in the boundary layer are modelled through the use of a zero-equation algebraic Cebici-Smith or Baldwin-Lomax eddy-viscosity model.

Program Structure

There are three programs which comprise the current airfoil analysis package. The boundary-layer and Euler codes are called SDGM and GAUSS2, respectively. The interaction of the inner and outer region flow solvers is accomplished by a third control code called VII. There are a number of input and output date files which are utilized by the three codes. The control code VII is the only code which is explicitly invoked from the command line, and VII consequently uses internal system calls to execute either GAUSS2 or SDGM to iteratively perform the viscous and inviscid flow calculations. GAUSS2 utilizes a cartesian C-grid to solve for the entire inviscid flowfield while SDGM uses a body-normal coordinate system to solve for the viscous flowfield on the upper and lower surfaces of the airfoil.

Data Files

The following figure shows all of the data files which are either read or written by the three codes. Arrows indicate whether the data is being read or written by the codes and indicates the interaction of data files between the codes. Many of the data files are used for interim data storage purposes and are not of particular interest to the end-user of the programs, but they are included here for completeness. The following is a list of data files which should be properly edited and available to the codes in order to start a flow analysis procedure:

	Filename	Description
1)	viinput.dat	input data used by VII to control overall viscous inviscid interaction process
2)	sdgminput1.dat	input data used by SDGM to control viscous flow calculations on upper surface of airfoil

3)	sdgminput2.dat	input data used by SDGM to control viscous flow calculations on lower surface of airfoil
4)	siminput1.dat	input data used by SDGM to control similarity solution calculations on upper surface of airfoil
5)	siminput2.dat	input data used by SDGM to control similarity solution calculations on lower surface of airfoil
6)	input	input data used by GAUSS2 to control inviscid flow calculations
7)	AIRGEO	input data used by GAUSS2 which contains inviscid C-grid

The following is a list of data files which contain the final output:

	Filename	Description
8)	convergence.dat	output data generated by VII which contains convergence history of aerodynamic force coefficients
9)	fcoeff.dat	output data generated by SDGM which contains skin-friction coefficient over the airfoil surface at streamwise locations based on the viscous marching algorithm
10)	bl2ext.dat	output data generated by SDGM which contains extrapolated integral quantities used in interaction algorithms at streamwise locations based on the inviscid grid
11)	pcoeff.dat	output data generated by GAUSS2 which contains pressure coefficient over the airfoil surface at streamwise locations based on the inviscid grid

Structure and Guidelines

The following is further definition of the necessary data files with an example format, variable definitions, and parameter guidelines:

1) viinput.dat

iinit
istart
iend
abschange1
abschange2

iinit - arbitrary starting number for global vii iterations (typically 1)
istart - number of iterations to wait before checking for convergence (typically 1/relax)
iend - maximum allowable number of global vii iterations (typically 50)
abschange1 - minimum absolute change in lift coefficient to signal vii convergence (typically 0.001)
abschange2 - minimum absolute change in total drag coefficient to signal vii convergence (typically 0.0001)

2) sdgminput1.dat

node
theta
pr
re
initx
totx
delx
transx
maxerror
extrb1
seprb1
relax

node - number of nodes in finite-element discretization (typically betwen 7 and 13)
theta - implicitness factor for crank-nicholson (typically 0.5)
pr - prandtl number (typically 1.0)
re - freestream reynolds number based on chord
initx - starting cartesian x/c location (typically 5.0 E-4)
totx - ending cartesian x/c location (typically 1.0)
delx - initial finite-difference marching step (typically 1.0 E-6)
transx - percent of cartesian x/c that transition to turbulence occurs
maxerror - maximum allowable ratio of the inverse shear stress nodal value and the change in the inverse shear stress nodal value (typically 1.0/(2^(node+2)))
extrb1 - maximum value of the inverse shear stress nodal value that indicates the onset of separation and the need to extrapolate future integral values (typically 10.0)
seprb1 - maximum value of the inverse shear stress nodal value that indicates separation (typically 100.0)
relax - vii relaxation parameter for the coupling mechanism (typically 0.1)

3) sdgminput2.dat - same as above

4) siminput1.dat

alphastart alphaend h eps
zguess(1) zguess(2) zguess(3) zguess(4)
ebctype
twto
m

alphastart - starting value of similarity parameter alpha (typically 0)
alphaend - asymptotic ending value of similarity parameter alpha (typically 10)
h - space width for similarity parameter alpha (typically 0.01)
eps - error tolerance for shooting method convergence (typically 1.0 E-5)

zguess(1) = lower bound for unknown momentum boundary condition (typically 1.93 for stagnation point flow)

zguess(2) = upper bound for unknown momentum boundary condition (typically 1.94 for stagnation point flow)
zguess(3) = lower bound for unknown energy boundary condition (typically -10*twto for adiabatic case)
zguess(4) = upper bound for unknown energy boundary condition (typically 10*twto for adiabatic case)
ebctype - flag to indicate type of energy wall-boundary condition (0=adiabatic, 1=heat transfer)
twto - ratio of wall and stagnation temperatures (typically 1.0)
m - falkner-skan pressure gradient factor where beta = (2*m)/(m+1) (typically 1.0 for stagnation point airfoil flows)

note: the most computationally efficient case is to set twto and pr = 1

5) siminput2.dat - same as above

6) input

alpha mach
cfl cflb ncyc iflaga iflagb sigma theta
connect darcy xp1 xp2 xp3 xp4
itedge mose xmax
ncycr

alpha = angle of attack in degrees
mach = freestream mach number
cfl = (typically 10.0)
cflb = local courant number (typically 1.0 E-3)
ncyc = number of total cycles (typically > 500)
iflaga = number of total cycles before shock fitting (typically 50)
iflagb = (typically 9999)
sigma = (typically 1.015)
theta = (typically 60.0)
connect = (typically 0)
darcy = (typically 0.0)
xp1 = (typically 1.0)
xp2 = (typically 1.0)
xp3 = (typically 1.0)
xp4 = (typically 1.0)
itedge = number of inviscid nodes from edge of inviscid grid to trailing edge of the airfoil (typically 14)
mose = (typically 1.58 E-2)
xmax = (typically 7.0)
ncycr = number of restart cycles (typically < 100)

7) AIRGEO - see example file